Article:
Zhao, Y, Hua, Y orcid.org/0000-0002-7457-1813, Liu, B et al. (5 more authors) (2021) The development of a Mechanistic-Chemometrics model with multi-degree of freedom for pitting corrosion of HP-13Cr stainless steel under extremely oilfield environments. Corrosion Science, 181. 109237. ISSN 0010-938X

https://doi.org/10.1016/j.corsci.2021.109237

The development of a Mechanistic-Chemometrics model with multi-degree of freedom for pitting corrosion of HP-13Cr stainless steel under extremely oilfield environments

Yang Zhao[1], Yong Hua[2], Bin Liu[3], Xuanpeng Li[4]*, Junfeng Xie[5], Guanxin Zeng[5], Tao Zhang[1]*, Fuhui Wang[1]

[1]*Shenyang National Laboratory for Materials Science, Northeastern University, 3-11 Wenhua Road, Shenyang 110819, China.*

[2]*Institute of Functional Surfaces, School of Mechanical Engineering, University of Leeds, Leeds, LS2 9JT, United Kingdom.*

[3]*Corrosion and Protection Laboratory, Key Laboratory of Superlight Materials and Surface Technology, Harbin Engineering University, Ministry of Education, Nantong ST 145, Harbin 150001, China.*

[4] *State Key Laboratory of Performance and Structural Safety for Petroleum Tubular Goods and Equipment Materials, Tubular Goods Research Institute, CNPC, Xi'an 710077, China*

[5] *Petrochina Tarim Oilfield Company, Shihua RD, Korla 841000, China.*

Corresponding authors: Xuanpeng Li (lixuanpeng127@163.com); Tao Zhang (zhangtao@mail.neu.edu.cn).

Abstract

A multi-degree of freedom mechanistic-chemometrics model for predicting the pitting damage of HP-13Cr stainless steel is developed by combining the mechanistic models and chemometrics method. The mechanistic model is reconstructed by considering the effect of single factors, such as high temperature, high CO_2 pressure, flow rates and complex stress distribution. The single mechanistic models are combined together considering the weight coefficients of variable interaction using the chemometrics method. Finally, the predicted results are validated by six-year-served field data, which indicates that the newly developed mechanistic-chemometrics model is accurate and highly reliable.

Keywords: A. Stainless steel; B. Modeling studies; B. Polarization; C. Pitting corrosion

1. Introduction

The increasing demand for resources has shifted the exploration towards ultra-deep oil wells at Tarim oilfield in the Northwest of China. Due to the complicated downhole conditions and geological characteristics in Tarim area [1-3], Oil Country Tubular Goods (OCTG) are in the oilfield environment (as depicted in Fig. 1). Fig. 1 represents the characteristics of complex oil-well environment, which is conducive to corrosion and can be described as [4]:

(1) Super corrosive media: the well depth reached 8000 m, high temperature (95 - 180 °C), high CO_2 pressure (2.8 - 3.8 MPa). The measured water cut was more than 30%. Moreover, the formation water contains high salinity (Cl^- concentration is about 60, 000 ppm).

(2) Stress Corrosion Cracking (SCC) mechanism: A neutral point, with zero stress above the packer, exists due to the gravity and mechanical properties of the structure tubing. Meanwhile, the tensile stress is located above the neutral point, while the stress transforms into compressive stress between the neutral point and the packer. Later on, due to the gravity, the compressive stress transforms into tensile stress below the packer [5].

HP-13Cr stainless steel (SS) is widely used as an OCTG in oil industry, as they offer improved CO_2 corrosion resistance in relation to carbon steels, and offer lower costs

than the duplex SS grades or Ni alloys [6-10]. However, the inspected field results have revealed that HP-13Cr SS suffers severe pitting corrosion. In general, the pitting corrosion can be divided into two processes, namely the pit initiation and the pit growth. The complex oilfield environment in terms of temperature, CO_2 pressure, flow rate and stress can influence the pitting processes. Nesic et al. [11] reported that temperature and CO_2 pressure accelerate the pitting corrosion by the electrochemical, chemical, and transport processes. Additionally, the effect of temperature and CO_2 pressure on the pitting corrosion has been studied on passive films and corrosion scales [6, 9, 10, 12-15]. The results illustrate that the enhanced pitting susceptibility of HP-13Cr SS can be attributed to the effects of temperature and CO_2 pressure on the microstructure and composition of corrosion scales [14]. In addition, Zhao et al. [15] discussed the influence of temperature and CO_2 pressure on the growth of pit on HP-13Cr SS. The results indicated that pit cavities grew deeper with the increase in temperature and CO_2 pressure from 95 °C / 2.8 MPa to 180 °C / 3.8 MPa after being immersed for 30 days.

Nesic et al. [11, 16] systematically studied the influence of flow rate on the carbon steel pipeline in the presence of CO_2 corrosion. It has been acknowledged that, high flow rate affects the CO_2 corrosion by increasing the mass transfer of corrosive species as well as damaging the corrosion scales. Schmitt et al. [17] indicated that 0.2 Pa of wall shear stress was enough to induce pitting corrosion. Moreover, Xu et al. [18] reported that flow rate can suppress the development of potential pits by

uniformly distributing ions at the interface of metal. Wharton et al. [19] reported that the flow rate (0.04- 2.7 m/s) had a negligible influence on pit nucleation and metastable pitting, whereas the growth of pits became obvious when the flow rate was slower than 1.5 m/s. Furthermore, these experimental results were confirmed by hydrodynamic and electrochemical noise measurements for AISI 304 SS. Wei et al. [20] proposed that the flow rate (0.5-2 m/s) accelerated the pitting corrosion by damaging the corrosion scales and inhibiting the formation of $FeCO_3$ on the surface of X70 under supercritical CO_2 environment. Recently, Zhao et al. [15] demonstrated that the flow rate altered the pitting geometry from bullet shape to shallow-disk shape at the flow rate of 3 m/s.

Moreover, it has been reported that the applied tensile stress increased the pitting susceptibility, whereas the compression stress could reduce the pitting susceptibility [21-26]. Iwanaga et al. [26] performed polarization tests and reported that pitting susceptibility of stainless steels increased with the increase in tensile stress. Vignal et al. [27] demonstrated that the local tensile stress gradient played a key role in accelerating the pit initiation process. Additionally, Feng et al. [28] proposed two degradation modes for the passive film under tensile or compressive stress. The results suggested that tensile stress produced micro-cracks, which were perpendicular to the surface, whereas the compressive stress induced de-bonding of the passive film from the steel substrate [28]. Moreover, Guo et al. [29] and Fatoba et al. [30] reported that, based on Gutman model, the influence of tensile stress on the acceleration of

111 metastable pit and pit growth based on Gutman model can be attributed to the
112 mechanical-electrochemical effect at the local plastic deformation around the bottom
113 of the pit [31].
114
115 Significant progress has been achieved in understanding the effect of temperature,
116 CO_2 pressure, flow rate and stress on the pitting corrosion [32-33]. However, the
117 synergistic effect of these factors on pitting corrosion of HP-13Cr SS has not yet been
118 studied in detail. The development of a theoretical model to predict corrosion damage
119 of HP-13Cr SS in the extremely oilfield environments has become necessary. In
120 recent years, CO_2 corrosion has been extensively investigated to understand the
121 fundamental corrosion mechanism, whereas corrosion prediction models have also
122 been developed to predict the CO_2-induced corrosion for various steels [11]. The
123 current prediction models, including empirical models [34, 35], semi-empirical
124 models [36-38], and comprehensive mechanistic models [39-41], mainly focus on
125 CO_2-induced general corrosion of mild steel. It should be noted that the pitting
126 corrosion plays a major role in the failure of wells. Therefore, a significant research
127 effort has been devoted to predict the pitting corrosion using the stochastic model and
128 deterministic model [42-46]. Recently, Zhang' group [47] proposed a novel model to
129 predict the pitting corrosion, which considers the influence of the initiation and
130 growth of a pit. The proposed model was based on a combination of Sridhar model,
131 Macdonald model, Weibull extreme value statistics and Gumbel extreme value
132 statistics method. The proposed model was successfully applied to predict the

development of pitting at various times for 304 SS. However, the modelling became a challenge for corrosion under complex coupling environments due to which, the model required further reconstruction.

In addition, chemometrics method belongs to a discipline that provides an efficient approach through statistical or mathematical methods to investigate the effect of each variable and the interaction between variables [48-50]. A combination of chemometric method and the model proposed by Zhang's group results in a novel mechanistic-chemometric prediction model, which is developed herein in order to incorporate the influence of temperature, CO_2 pressure, flow rate and stress on the growth kinetics of pits. The model has then been used to perform pitting corrosion calculations. In order to verify the accuracy of mechanistic-chemometric model, the predicted results are compared with the field data of HP-13Cr SS well after being used for six years in the Tarim area.

2. Experimental

2.1 Materials

HP-13Cr SS was used in the current study, and had the composition of (wt. %) Si (0.15), Mn (0.51), Cr (12.77), Mo (2.19), S (0.002), P (0.02), Cu (0.047), Ni (5.36), V (0.014), Al (0.037) and Fe (balance). The formation water was prepared by using the analytical grade reagents and distilled water. The compositions of various materials are listed in Table 1. The specimens of 50 mm × 5 mm × 3 mm (Fig. 2 (a)) were used

for the immersion and electrochemical tests under various temperatures and pressures. As shown in Figs. 2 (b-d), the specimen had the dimensions of 32 mm × 10 mm × 1 mm and was designed to investigate the pit growth process under different flow rates, tensile stresses and compressive stresses. In addition, based on the factorial design method [51], heteromorphic electrode was used to determine the weight coefficient. Prior to the testing, the specimen surface was ground by silicon carbide (SiC) paper up to 2000 grit. The formation water was deoxygenated with N_2 for 4 h. Then, 3.5 L formation water was introduced into the autoclave, sealed, and continuously bubbled with CO_2 at ambient temperature and pressure for 2 h to remove oxygen in the autoclave. Subsequently, the autoclave was heated to the required temperature, and high-pressure CO_2 was added to the autoclave using a booster pump.

2.2 Computational fluid dynamics and stress distribution

Herein, computational fluid dynamics (CFD) simulation of the flow distribution of heteromorphic electrode in the closed system was performed using the ANSYS FLUENT 14.0. A simulation geometry was constructed based on the dimensions of heteromorphic electrode and a tetrahedral computational 13000 element mesh was generated. Reynolds number (Re) is about 64,000 were in this experiment based on the fluid theory [52]. The SST k–ω turbulent model was used to approach the governing equations with an enhanced wall treatment. A uniform velocity-inlet boundary condition was selected, and a pressure-outlet boundary condition was set with a gauge pressure of zero for the closed system. The iterative calculations of the

177 semi-implicit method for pressure-linked equations (SIMPLE) algorithm were used to
178 solve the momentum equations (*N-S* equations), which modified the pressure term in
179 the discretized *N–S* equations and simultaneously renewed the velocity and pressure
180 field. The simulations were converged when the minimum value reached less than
181 5×10^{-4} [52-53].
182
183 In addition, the stress distribution was carried out using the COMSOL
184 MULTIPHYSICS 3.5a. A static solid stress-strain isotropic elastic analysis module
185 was used to simulate the stress distribution of high throughput tensile stress
186 heteromorphic specimens. Based upon the literature, the maximum applied stress (350
187 MPa) was lower than the yield strength (800 MPa) [5, 54].
188

189 **2.3 Methods**

190 The influence of each factor was quantified by 2^3 factorial design [54]. The lower and
191 upper values for temperature/CO_2 pressure, flow rate and stress were selected based
192 on the depth of well (Fig.1), and are presented in Table 2. The values of -1 and +1
193 indicated low and high levels for each factor. Meanwhile, after being immersed for
194 720 h, the maximum pitting depth (D_{max}) of HP-13Cr SS was taken as the response.
195 The multiple regression analysis through least-squares method was used to describe
196 the relationship between the factors (x) and responses (D_{max}). Moreover, the analysis
197 of variance (ANOVA) was performed to statistically evaluate the significance of
198 various factors. ANOVA was also used to test the null hypothesis. This method is

based on the decomposition of total variability in the selected response (y) and assesses the relationship between the factors and the variability of responses. The significant factors or interactions can be identified as the ratio of the mean square of a factor or as an interaction and the residual mean square (F-value) [49-50]. If the F-value was less than 11.27, the factors were considered as negligible [55].

2.4 Electrochemical characterization

The electrochemical measurements were carried out using a standard three-electrode system within the high-temperature high-pressure autoclave, as reported in some previous works [14-15]. HP-13Cr SS was used as a working electrode, whereas platinum was used as a counter electrode. Furthermore, an external pressure balanced Ag/AgCl was used as the reference electrode (0.1 M KCl solution). The electrode potentials were converted to standard hydrogen electrode (SHE) potential using Equation (1) [56].

$$E_{\mathrm{SHE}} = E_{\mathrm{obs}} + 0.2866 - 0.001(T - T_0) + 1.754 \times 10^{-7}(T - T_0)^2 - 3.03 \times 10^{-9}(T - T_0)^3 \quad (1)$$

where E_{SHE} represents the electrode potential *vs* SHE, E_{obs} represents the measured electrode potential *vs* the Ag/AgCl reference electrode (V), T refers to the experimental temperature (°C) and T_0 denotes the room temperature (25 °C).

The specimens were potentiostatically polarized at -1.3 V_{SHE} for 3 min to remove the surface oxide layer. The re-passivation potential (E_{rp}) was measured using the cyclic

potentiodynamic polarization measurements according to ASTM G61-86 [57]. The cyclic potentiodynamic polarization curves were recorded from a potential of -100 mV vs the Open Circuit Potential (OCP). When the increased potential was up to a current density of 1 mA/cm^2 with the scan rate of 1 mV/s, the scan was reversed to obtain the E_{rp}. Then, the scan rates were changed through values of 0.5 mV/s, 0.333 mV/s and 0.167 mV/s. The temperature and pressure of electrochemical tests were maintained at 95 °C/2.8 MPa, 120 °C/3.2 MPa, 150 °C/3.6 MPa and 180 °C/3.8 MPa. For each electrochemical test, the measurement was repeated at least three times.

2.5 Immersion tests

Immersion experiments were performed in a 5-L high-temperature and high-pressure autoclave. A schematic of the experimental setup can be viewed in our previous study [15]. Similar to the previous study [15, 47], the specimens were immersed in 6 wt. % $FeCl_3$ solution for 20 s at 30 °C to eliminate the pit initiation time prior to immersion experiments according to the ASTM G48-2000 [58]. After the pre-initiated pits, the specimens were ultrasonically cleaned in acetone for 3 min and dried in cold air. The specimens were fixed to the rotating cage and immediately immersed into the autoclave.

The heteromorphic electrode was designed to investigate the pit growth at various flow rates [59]. Fig. 3 shows the flow distribution at the surface of the heteromorphic electrode, whereas the corresponding results are presented in Table 3. When the flow

243 rate of the marked surface 6 was controlled at 1 m/s, the marked surfaces 1, 2, and 5
244 experienced the flow rates of 0.31 m/s, 0.5 m/s and 0.72 m/s, respectively. The
245 bump-shaped specimens were evenly arranged around the central axis of the rotating
246 cage and mounted within the autoclave.
247
248 A schematic of the corrosion rotating cage with various stress levels is displayed in
249 Fig. 4. The calculated tensile stress distribution is shown in Fig. 5(a). The finite
250 element analysis results showed that various tensile stresses for different width
251 sections could be achieved. For the Surface-3, the tensile stress was fixed at 350 MPa,
252 whereas the tensile stresses of 210 MPa, 175 MPa and 270MPa were set for
253 Surfaces-1, -2, and -4, respectively. In addition, the tensile stress and flow rate
254 distribution of T-type flat specimen are shown in Figs. 5(b) and 5(c). The constant
255 tensile stress area exhibited a stable flow rate, which indicated that the T-type sample
256 and the stress corrosion rotating cage could be used to simulate the stress, flow rate
257 and the coupling experiments.
258
259 According to the experimental design presented in Table 4, the immersion
260 experiments were performed at various temperatures/CO_2 pressures, flow rates, and
261 stresses using the stress corrosion rotating cage with T-type tensile stress specimens
262 for 30 days. Four independent specimens were used to measure the maximum pitting
263 depth in each experiment.
264

After the experiments, the specimens were ultrasonically cleaned in acetone for 5 min. Then, the specimens were dried using cold air and stored in a desiccator before measuring the pit depth. The morphology of the pits was determined using an OLS4100 confocal laser scanning microscope. The maximum pit depth was recorded. Meanwhile, the Gumbel distribution was used to model the behavior of maximum pitting depth. The cumulative probability $F(\mathrm{Y})$ of the maximum pitting depth can be given by Equation (2) [47, 60].

$$F(\mathrm{Y}) = \exp\{-\exp\left[-\left(\frac{D_{max}-\mu}{\lambda}\right)\right]\} \quad (2)$$

where D_{max} represents the maximum pitting depth, μ refers to the central parameter (the most frequent value) and λ denotes the scale parameter. The two parameters μ and λ are calculated from the relationship of reduced variant (Y) and D_{max}, where Y can be calculated using the correlation: $Y = -\ln\{-\ln[F(\mathrm{Y})]\}$.

2.6 Field data measurement

The corroded tubing over the past six-years was collected in Tarim. Along the well profile, the maximum pit depth of HP-13Cr SS was monitored using a micrometer pit depth gauge attached to a bridging bar. The tubing was cut into small pieces (50 mm × 50 mm). The specimens were ultrasonically cleaned in acetone for 5 min, and pitting depth was measured using the OLS4100 confocal laser scanning microscope.

3. Results and discussion

3.1 Pit initiation time

287 According to a previously proposed pit initiation model [47], the schematic of the
288 pitting corrosion is shown in Fig. 6. The t_{init} was related to the applied potential (E_{app}),
289 open circuit potential (E_{ocp}) and the E_{rp}, whereas it was equal to the intersection point
290 of the E_{app}-E_{rp} and E_{ocp}-E_{rp}.
291
292 **3.1.1 Determination of E_{rp}**
293 As reported in Zhang's group previous work and Sridhar's model, E_{rp} can be regarded
294 as the critical potential to predict the pitting corrosion. The relationship between
295 pitting potential (E_{pit}) [43, 47, 61], E_{rp} and square root of the potential sweep rate ($v^{1/2}$)
296 was obtained through the cyclic potentiodynamic polarization tests. The potential
297 sweep rate was nearly zero throughout the service-life of HP-13Cr SS. Therefore, at
298 zero potential sweep rate, the E_{rp} and E_{pit} of HP-13Cr SS need to be corrected under
299 different temperatures and CO_2 pressures.
300
301 Fig. 7 displays the cyclic potentiodynamic polarization curves for HP-13Cr SS under
302 various temperatures and CO_2 pressures. The curves were drawn under different scan
303 rates and the values of E_{pit} and E_{rp} are summarized in Table 5. Both the E_{pit} and E_{rp}
304 decreased with the increase of scan rate. Meanwhile, E_{pit} and E_{rp} shifted towards the
305 cathodic direction with the increase in temperature and pressure. The minimum values
306 of 152.66 ± 3.13 mV_{SHE} and -212.38 ± 0.78 mV_{SHE} were obtained at 180 °C/3.8 MPa.
307 It can be noted that E_{pit} and E_{rp} linearly increased with the square root of sweep rate
308 ($v^{1/2}$) under various temperatures and CO_2 pressures, as shown in Fig. 8. Meanwhile,

the value of E_{pit} and E_{rp} at the sweep rate of 0 mV/s could be predicted [62], as presented in Table 4.

3.2 Evolution of the OCP

The monitored OCP for various immersion times can be used to predict the occurrence of pitting [43]. The OCP evolution with time can be described using Equation (3) [43, 63].

$$E = E_{oc} - \frac{1}{\gamma}\ln\left[\frac{-B\gamma}{A}t + \exp[-\gamma(E_{corr} - E_{oc})]\right] \quad (3)$$

where γ represents the Tafel constant for the cathodic electrode reaction, E_{oc} refers to the cathodic electrode reaction equilibrium potential, and A and B are the constants and their values are related to the naturally formed passive film.

The equation proposed by Burstein et al. (Equations (4)-(5)) [64-65] indicates that the proposed OCP evolution (as given by Equation (3)) considers the nature of passive film formed on stainless steel. Therefore, the Equation (3) allows for extrapolation of passive film formed on HP-13Cr SS under various temperatures and CO_2 pressures.

$$E = A_1 \ln t + B_1 \quad (4)$$

$$E = E_{oc} - A_2 - \frac{1}{\gamma}\ln t \quad (5)$$

where A_1 and B_1 refer to the fitting parameters, which depend on the pH value, and A_2 is a constant. In order to predict the OCP evolution at various temperatures and CO_2 pressures, some critical parameters are listed in Table 6. The γ and i_o can be calculated from the cathodic polarization curves based on the Butler-Volmer equation. Additionally, the values of the electric field strength (ε_L), E_{oc} and the Point Defect

Model (PDM) parameters were taken from our previous work [14, 47]. Therefore, OCP changes with immersion time under various temperatures and CO_2 pressures, as described by Equations (6)-(9).

$$E\ (\mathrm{mV_{SHE}}) = -182.7 + 89.36 \times \ln(0.028 \times t + 0.354) \quad (95\ ^\circ\mathrm{C}/\ 2.8\mathrm{MPa}) \tag{6}$$

$$E\ (\mathrm{mV_{SHE}}) = -155.1 + 92.67 \times \ln(0.018 \times t + 0.253) \quad (120\ ^\circ\mathrm{C}/\ 3.2\mathrm{MPa}) \tag{7}$$

$$E\ (\mathrm{mV_{SHE}}) = -117.0 + 97.37 \times \ln(0.01 \times t + 0.135) \quad (150\ ^\circ\mathrm{C}/\ 3.6\ \mathrm{MPa}) \tag{8}$$

$$E\ (\mathrm{mV_{SHE}}) = -72.8 + 91.07 \times \ln(0.072 \times t + 0.051) \quad (180\ ^\circ\mathrm{C}/\ 3.8\ \mathrm{MPa}) \tag{9}$$

The calculated OCP values are displayed in Fig. 9. The values increase continuously over time, which is consistent with the measured data [66]. The results show that the OCP values exceeded E_{rp} after 38.4 days, 22.2 days, 21.7 days, and 18.1 days under the temperature/pressure of 95 °C/2.8 MPa, 120 °C/3.2MPa, 150 °C/3.6 MPa and 180 °C/3.8 MPa, respectively.

3.3 Pit induction time (t_{ind}) above E_{rp}

The relationship between the pit induction time (t_{ind}) and the applied potential (E_{app}) can be given by Equation (10) [47].

$$t_{\mathrm{ind}} = a \exp(-b \cdot \Delta E) + c \tag{10}$$

where a, b, and c are constants, and ΔE represents the difference between E_{app} and $E_{rp(v=0)}$. Fig. 10 shows the time dependence of current density on a logarithmic scale for HP-13Cr SS immersed in the formation solution at various applied potentials. The turning point in Fig. 10 between the passive stage and the pit growth changed, suggesting that t_{ind} was highly influenced by temperatures and pressures. As shown in Fig. 10, t_{ind} decreased with the increase in the value of ΔE. Fig. 11 indicates that the

values of a, b, and c decreased with the increase in temperature and CO_2 pressure. However, the pit initiation time (t_{init}) cannot be regarded as a simple sum of $t_{OCP \to E_{rp}}$ and t_{ind}. Based upon our previous work [47], t_{init} can be obtained using Equation (11).

$$\begin{cases} E = E_{oc} - \frac{1}{\gamma}\ln\left[\frac{-B\gamma}{A}t_{init} + \exp[-\gamma(E_{corr} - E_{oc})]\right] \\ t_{init} = t_{OCP \to E_{rp}} + a\exp\left[-b \cdot \left(E - E_{rp(v=0)}\right)\right] + c \quad \left(E > E_{rp}\right) \end{cases} \tag{11}$$

Graphical method is used to calculate the value of t_{init} and the corresponding results under different temperatures and pressures are presented in Fig. 12. With the increase in temperature and pressure from 95 °C/2.8 MPa to 180 °C/3.8 MPa, the t_{init} values were 76.8 days, 39.7 days, 34.6 days, and 28.6 days, respectively. In addition, several researchers concluded that the flow rate and stress played a significant role in accelerating the t_{init} [11-30]. Moreover, the maximum t_{init} was far shorter than the required design service life-time (15 years) for HP-13Cr SS under the current conditions. The critical factor determining the life-time was the pitting growth process. Herein, the correction of t_{init} by the flow rate and stress could be neglected. Based upon Fig. 1, the temperature and CO_2 pressure increased with the depth of the well. Therefore, the relationship between t_{init} and temperature/CO_2 pressure can be transformed into t_{init} and the depth of well. The results are shown in Fig. 13, whereas nonlinear fitting equation is given by Equation (12).

$$t_{init} = 30.20+130.61\times\exp(-1.29\times Depth(\text{km})) \tag{12}$$

3.2 Mechanistic model for the single factor

For HP-13Cr SS, t_{init} of 76.8 days was obtained for 95 °C/2.8 MPa, which is too long

376 to investigate the pit growth. In the present work, the pre-initiated pits on HP-13Cr SS
377 were used to study the pit initiation time. The cumulative probability plot and the
378 Gumbel plot of the maximum pit depth were drawn from 20 specimens after
379 pre-initiated pits, as shown in Fig. 14. The fitted Gumbel distribution (red in Fig. 14)
380 was fairly consistent with the experimentally measured maximum pit depth. The
381 location parameter (μ) and the scale parameter (λ) were found to be 8.28 μm and 0.97,
382 respectively. Moreover, the typical morphologies of the pits after pre-initiation are
383 shown in Fig. 15. The growth of pit after pre-initiated pits on HP-13Cr SS can be
384 described using Equation (13) [47].

385 $$D_{\max} = K[t + (t_0 + t_{\text{init}}) - t_{\text{init}}]^{\omega} = K(t + t_0)^{\omega} \quad (13)$$

386 where t_o refers to the pit growth time. Furthermore, the mechanistic model for pit
387 growth under various temperatures, CO_2 pressures, flow rates, and stress levels will
388 be discussed in detail in the following paragraphs. The morphologies of the maximum
389 pit and the Gumbel plots under various condition are shown in Appendix 1.

390

391 **3.2.1 Mechanistic model for temperature/CO_2 pressure**

392 Fig. 16 shows the Gumbel plots of the maximum pit depths measured for ten
393 specimens at various temperatures and CO_2 pressures. It is worth noticing that the
394 fitted Gumbel distribution shifted to the right and rotated clockwise with the increase
395 in immersion time, which is in good agreement with the previously reported data [67].
396 In addition, the local parameter (μ) and scale parameter (λ) are presented in Table 7.
397 Moreover, the time-dependence of the averaged maximum pit depth under various

temperatures and CO_2 pressures is presented in Fig 17. The variation of the averaged maximum pit depth with time can be fitted using Equation (12). With the increase in temperatures and CO_2 pressures, the pit proportionality (K) increased from 4.53 to 13.46, whereas the pitting exponent (ω) increased from 0.417 to 0.487 (following Eq. 14). Therefore, the results revealed that the growth rate of pit increased with the increase in temperature and CO_2 pressure. Moreover, one should notice that ω was located within the range of 0.417 - 0.487. When the ω was about 0.5, the pit growth was controlled by diffusion [68]. The depth of pits increased with the increase in temperature and CO_2 pressure, while the typical pit morphologies are shown in Fig. S1 (Appendix 1). In addition, the relationship between the pit growth parameters and the well depth are provided in Fig. 18.

$$\begin{cases} K = 4.46 + 0.26 \times \exp(0.44 \times depth) \\ \omega = 0.37 + 0.05 \times \exp(0.12 \times depth) \end{cases} \quad (14)$$

The maximum pit depth can be calculated using Equation (15).

$$D_{\max} = [4.46 + 0.26 \times \exp(0.44 \times depth)] \times t^{0.37+0.05\times\exp(0.12\times depth)} \quad (15)$$

3.2.2 Effect of the flow rate on the mechanistic model

As shown in Fig. S2 (Appendix 1), the Gumbel distribution describes the maximum pit depth under various flow rates. Fig. 19 shows the development of averaged maximum pit depth, which was fitted from the Gumbel plots (as displayed in Table S1 (Appendix 1)). It can be seen that the maximum pit depth gradually decreased with the increase in flow rate within the range of 0.31-1 m/s. Furthermore, the growth kinetics of pits was fitted using Equation (10), and the results show that the value of K

decreased from 4.86 to 3.70 when the flow rate increased from 0.31 m/s to 1 m/s. The decrease in growth rate of the pit was mainly attributed to the vortex generated inside the pit, where the distribution of H^+ and metal ion was inhomogeneous [15]. The pit morphologies are displayed in Fig. S3 (Appendix 1), indicating that the presence of vortex accelerated the pit growth in the horizontal direction and formed the shallow-disk shape pit on the surface of HP-13Cr SS.

Fig. 20 exhibits the relationship between K and flow rate (V) using Equation (16).

$$K = -2.93 \times \exp(0.43 \times V) + 8.15 \quad (16)$$

Then, the D_{max} for the flow rate can be described using Equation (17).

$$D_{\max} = [-2.93 \times \exp(0.43 \times V) + 8.15] \times t^{0.42} \quad (17)$$

3.2.3 Effect of stress on the growth of pit

Based upon the results presented in Fig. 1, it can be noted that there was a transition between the tensile stress and the compressive stress along the well's depth. The stress distribution can be calculated based on the pipe mechanics using Equation (18).

$$\begin{cases} F = -0.088d + 425.93 & (\text{tensile stress}, d \le 5000m) \\ F = -0.088d + 425.93 & (\text{compress stress}, 5000m \le d \le 7500m) \\ F = -0.078d + 624 & (\text{tensile stress}, 7500m \le d \le 8000m) \end{cases} \quad (18)$$

The tensile stress and the compressive stress accompany a positive and a negative sign, respectively.

Fig. 21(a) indicates that the maximum pit depth increased significantly with the increase in tensile stress due to the mechanical-electrochemical effect, which is consistent with some previous studies [30-31]. The relationship among K, ω and

stress can be expressed using Equations (19) and (20).

$$K = \begin{cases} 0.016 \times \exp(-0.012 \times F) + 5.47 \text{ (tensile stress)} \\ -0.09 \times \exp(-0.0056 \times F) + 5.40 \text{ (compression stress)} \end{cases} \quad (19)$$

$$\omega = \begin{cases} 0.041 \times \exp(0.0026 \times F) + 0.40 \text{ (tensile stress)} \\ 0.44 \qquad\qquad\qquad\quad \text{(compression stress)} \end{cases} \quad (20)$$

The pit morphologies are displayed in Fig. S5 (Appendix 1) and suggested that a large pit was formed on the surface under the effect of tensile stress. However, the increase in compressive stress within the range of 0-250 MPa represented a limited effect on the growth rate of a pit, as shown in Fig. 21(b). The values of K and ω with respect to the stress are presented in Fig 22. It can be noticed that the turning point appeared at F = 0 MPa (Fig 22(a)). However, the differences between the compressive and tensile stress values in terms of ω values can be neglected. For the compressive stress, ω remained around 0.44, whereas ω gradually increased from 0.453 to 0.493 as the tensile stress increased from 175 MPa to 350 MPa. Therefore, the D_{max} value under the impact of stress bounced back following Equation (13), and the relationship can be expressed using Equations (21) and (22).

For tensile stress (0 - 350 MPa):

$$D_{\max} = [0.016 \times \exp(-0.012 \times F) + 5.47] \times t^{0.041 \times \exp(0.0026 \times F) + 0.40} \quad (21)$$

For compressive stress (0 - -250 MPa):

$$D_{\max} = [-0.09 \times \exp(-0.0056 \times F) + 5.40] \times t^{0.44} \quad (22)$$

3.3 Multi-degree of freedom model for predicting pitting damage under complex

oilfield environment

The mechanistic-chemometrics model proposed in this work can be divided into two processes: (*i*) the mechanistic-model under different factors, (*ii*) Combining the single factor mechanistic-model using the weight coefficients of each factor and their mutual interactions. A combination of weight coefficients and sub-model to formulate the pit prediction model can be described using Equation (23).

$$D_{\max} = \sum_{\mathrm{i}} f_{\mathrm{i}} K_{\mathrm{i}} (t - t_{\mathrm{init}})^{\omega_{\mathrm{i}}} \quad (23)$$

where *i* refers the influencing factors, and includes temperature, CO_2 pressure, flow rate, stress and interaction of each factor with others. Moreover, f_{i} represents the weight coefficient of i^{th} factor, and K_{I} and ω_{I} represent the pit proportionality and exponent of i^{th} factor, respectively.

3.3.1 Determination of the weight coefficient using chemometrics method

Table 2 summarizes the designed experiments and presents the measured maximum pit depth on the surface of HP-13Cr SS after being immersed in CO_2-saturated formation water for 30 days. The pit morphologies are displayed in Fig. S8 (Appendix 1). The relationship between the maximum pit depth and the influencing factors using the statistical regression analysis can be given by Equation (24).

$$D_{max} = 13.09 + 6.52x_1 - 0.80x_2 + 3.50x_3 - 0.54x_1x_2 + 2.39x_1x_3 - 0.18x_2x_3 - 0.076x_1x_2x_3 \quad (24)$$

where x_1, x_2, and x_3 represent the influencing factors (temperature/pressure, flow rate, and stress, respectively), and $x_i x_j$ (i and j = 1, 2, 3) represents the interaction terms. Moreover, the influence of various factors and the interactions on the maximum pit depth were further justified using the ANOVA analysis.

As shown in Fig. 23, temperature/CO_2 pressure is the most significant factor, followed by the stress and the combined influence of temperature/CO_2 pressure and stress. The effect of a given factor became significant if its F-value was higher than the critical value of 11.26. The flow rate and interactions among factors were not significant for the pitting corrosion in the complex oil field environment. The regression model can be simplified as Equation (25).

$$D_{max} = 13.09 + 6.52x_1 + 3.50x_3 + 2.39x_1x_3 \quad (25)$$

The Pareto analysis is proposed as a quantitative method to determine the weight coefficients of the maximum pit depth, as given by Equation (26) [50].

$$P_i = \left(\frac{a_i^2}{\sum_{i\neq 0} a_i^2}\right) \times 100\% \quad (26)$$

where P_i refers to the percentage effect of each variable on pit depth and a_i represents the coefficient of each variable. The results of Pareto analysis are shown in Fig. 23. It can be noted that the temperature/pressure are the most significant factors, followed by stress, and stress interaction, with the corresponding weight coefficients of 52.54%, 28.20%, and 19.26%, respectively.

3.3.2 Validation of the model with field data

Based on Equation (22), the mechanistic-chemometrics model can be described as

508 Equation (27).

509

510
$$\begin{cases} t_{\text{ind}} = 52.54\% \times t_{T/P} - 28.20\% \times t_F - 19.26\% \times (t_{T/P} \times t_F) \\ K = 52.54\% \times K_{T/P} + 28.20\% \times K_F + 19.26\% \times (K_{T/P} \times K_F) \\ \omega = 52.54\% \times \omega_{T/P} + 28.20\% \times \omega_F + 19.26\% \times (\omega_{T/P} \times \omega_F) \end{cases} \quad (27)$$

511

512 The maximum pit depths are summarized in Table 2. Valor et al. [65], Provan et al.
513 [69], and Cavanaugh et al. [70] reported that the growth kinetics of pits can be
514 simplified as $D_{\max} = Kt^{\omega}$, when the t_{init} is small compared to the immersion time,
515 and suggested that the t_{init} can be neglected in predicting the long-term pit damage for
516 HP-13Cr SS under complex oilfield environment.

517

518 In order to verify the accuracy of the model for a complex oil environment, the
519 maximum pit depth formed on HP-13Cr SS was measured after 6 years in service.
520 The maximum pit depth along the depth of the well is displayed in Fig. 24. It can be
521 seen clearly that the pit depth initially decreased with the increase in the depth of the
522 well, followed by a sharp increase. The results also indicate that the maximum pit
523 depths were found near the top and bottom of the well. As a comparison, the predicted
524 maximum pit depth along the well profile is shown in Fig. 24. The proposed
525 mechanistic-chemometrics model is highly reliable in predicting the pitting damage
526 and can be utilized in current oilfield environments.

527

528 **4. Conclusions**

529 The multi-degree of freedom model has been developed to predict the pit behavior
530 under complex oilfield environment using a combination of weight coefficients and
531 sub-models of temperature/pressure, flow rate and stress. Based upon the results,
532 following conclusions are drawn.
533
534 (1) The t_{init} value decreased with the increase in temperature/CO_2 pressure, and the
535 correction of t_{init} by flow rate and stress could be neglected. Finally, the
536 relationship between t_{init} and temperature/CO_2 pressure can be applied to the
537 whole depth of the well.
538
539 (2) The growth rate of a pit is accelerated with the increase in temperature/CO_2
540 pressure, flow rate and tensile stress. Moreover, the compressive stress shows a
541 negligible effect on the growth of pit.
542
543 (3) For a chemometrics method, two-level factorial design is performed to identify the
544 most significant factors and interactions influencing the pit depth formed on the
545 HP-13Cr SS surface under complex oilfield environments. The temperature/CO_2
546 pressure, stress and their interactions were identified as the most significant factors
547 in terms of pit depth, and the weight coefficients were determined to be 52.54%,
548 28.20% and 19.26%, respectively.
549
550 (4) The measured data from Tarim area. in China confirmed the reliability of the

proposed model for predicting the pitting behavior of HP-13Cr SS oil tubes under complex oilfield environment.

Data availability

The raw/processed data required to reproduce these findings cannot be shared at this time, as the data form part of another ongoing study.

Authorship contribution statement

Yang Zhao: Investigation, Writing - original draft. **Yong Hua**: Investigation, Visualization, Writing - review and editing. **Bin Liu**: Investigation, Funding acquisition. **Xuanpeng Li**: Conceptualization, Writing - review and editing, Funding acquisition. **Junfeng Xie**: Writing - review and editing. **Guanxin Zeng**: Writing - review and editing. **Tao Zhang**: Conceptualization, Writing - review and editing, Funding acquisition. **Fuhui Wang**: Writing - review and editing.

Acknowledgements

The authors wish to acknowledge the financial support provided by the National Key Research and Development Program of China (Grant No.: 2017YFB0702203), the National Natural Science Foundation of China (Grant No. U1460202), the National program for the Young Top-notch Professionals, the Fundamental Research Funds for the Central Universities (Grant No.: N170205002) and the Key Laboratory of Superlight Material and Surface Technology (Harbin Engineering University, China),

573 Ministry of Education, China and the Chinese Postdoctoral Science Foundation
574 (Grant No.: 01270012810066).

575

576 **References**

577 [1] H. Pang, J.Q. Chen, X.Q. Pang, L.F. Liu, K.Y. Liu, C.F. Xiang, Key factors
578 controlling hydrocarbon accumulations in Ordovician carbonate reservoirs in the
579 Tazhong area, Tarim basin, western China, Mar. Petrol. Geol. 43 (2013) 88 - 101.
580 [2] P. Li, Y Zhao, B. Liu, G.X. Zeng, T. Zhang, D.K. Xu, H. Gu, T.Y Gu, F.H. Wang,
581 Experimental testing and numerical simulation to analyze the corrosion failures of
582 single well pipelines in Tahe oilfield, Eng. Fall. Anal. 80 (2017) 112 - 122.
583 [3] C.I. Ossai, B. Boswell, I.J. Davies, Pipeline failures in corrosive environments - a
584 conceptual analysis of trends and effects, Eng. Fail. Anal. 53 (2015) 36 - 58.
585 [4] Y. Zhao, W.L Qi, J.F. Xie, Y. Chen, T. Zhang, D.K. Xu, F.H. Wang, Investigation
586 of the failure mechanism of the TG-201 inhibitor: Promoting the synergistic effect of
587 HP-13Cr stainless steel during the well completion, Corros. Sci. 166 (2020) 108448.
588 [5] X.T. Yang, X.P. Shen, X.H. Cui, K.L. Wang, G.Y. Shen, Z.B. Wang, T. Qin, Stress
589 and deformation characteristics of completion and testing tubing string with
590 expansion joints for ultra-deep HTHP gas wells, Natural. Gas. Industry. B. 7 (2020)
591 101-108.
592 [6] X. Yue, L. Zhang, Y. Wang, S. Xu, C. Wang, M. Lu, A. Neville, Y. Hua, Evolution
593 and characterization of the film formed on super 13Cr stainless steel in CO_2-saturated
594 formation water at high temperature, Corros. Sci. 163 (2020) 108277.

595 [7] X.W. Lei, Y.R. Feng, A.Q. Fu, J.X. Zhang, Z.Q. Bai, C.X. Xin, C.H. Lu,
596 Investigation of stress corrosion cracking behavior of super 13Cr tubing by full-scale
597 tubular goods corrosion test system, Eng. Fail. Anal. 50 (2015) 62-70.
598 [8] Y. Zhao, J. Xie, G. Zeng, T. Zhang, D. Xu, F. Wang, Pourbaix diagram for
599 HP-13Cr stainless steel in the aggressive oilfield environment characterized by high
600 temperature, high CO_2 partial pressure and high salinity, Electrochim. Acta. 293 (2019)
601 116 – 127.
602 [9] R.M. Moreira, C.V. Franco, C.J.B.M. Joia, S. Giordana, O.R. Mattos, The effects
603 of temperature and hydrodynamics on the CO_2 corrosion of 13Cr and 13Cr5Ni2Mo
604 stainless steels in the presence of free acetic acid, Corros. Sci. 46 (2004) 2987 - 3003.
605 [10] T. Sunaba, T. Ito, Y. Miyata, S. Asakura, T. Shinohara, T. Yakou, Y. Tomoe, H.
606 Honda, Influence of chloride ions on corrosion of modified martensitic stainless steels
607 at high temperatures under a CO_2 environment, Corrosion. 70 (2014) 988 - 999.
608 [11] S. Nesic, Key issues related to modelling of internal corrosion of oil and gas
609 pipelines - A review, Corros. Sci. 49 (2007) 4308 - 4338.
610 [12] L.J. Mu, W.Z. Zhao, Investigation on carbon dioxide corrosion behaviour of
611 HP13Cr110 stainless steel in simulated stratum water, Corros. Sci. 52 (2010) 82-89.
612 [13] H. Zhang, Y. L. Zhao, Z. D. Jiang, Effects of temperature on the corrosion
613 behavior of 13Cr martensitic stainless steel during exposure to CO_2 and Cl^-
614 environment, Mater. Lett. 59 (2005) 3370-3374.
615 [14] X.P. Li, Y. Zhao, W.L. Qi, J.D. Wang, B. Liu, G.X. Zeng, T. Zhang, F.H. Wang,
616 Effect of extremely aggressive environment on the nature of corrosion scales of

617 HP-13Cr stainless steel, Appl. Sur. Sci. 469 (2019) 146 -161.
618 [15] Y. Zhao, X. Li, C. Zhang, T. Zhang, J. Xie, G. Zeng, D. Xu, F. Wang,
619 Investigation of the rotation speed on corrosion behavior of HP-13Cr stainless steel in
620 the extremely aggressive oilfield environment by using the rotating cage test, Corros.
621 Sci. 145 (2018) 307–319.
622 [16] S Nesic, Effects of multiphase flow on internal CO_2 corrosion of mild steel
623 pipelines, Energ. Fuel. 26 (2012) 4098-4111.
624 [17] G. Schmitt, M. Mueller, Critical Wall Shear Stresses in CO_2 Corrosion of Carbon
625 Steel, Corrosion/1999, NACE International, Houston/TX, 1999 paper no. 44.
626 [18] L.N. Xu, S.Q. Guo, W. Chang, T.H. Chen, L.H. Hu, M.X. Lu, Corrosion of Cr
627 bearing low alloy pipeline steel in CO_2 environment at static and flowing conditions,
628 Appl. Surf. Sci. 270 (2013) 395-404.
629 [19] J.A. Wharton, R.J.K. Wood, Influence of flow conditions on the corrosion of
630 AISI 304L stainless steel, Wear. 256 (2004) 525–536.
631 [20] L. Wei, X.L. Pang, K.W. Gao, Effect of flow rate on localized corrosion of X70
632 steel in supercritical CO_2 environments, Corros. Sci. 136 (2018) 339–351.
633 [21] X.Z. Wang, H. Luo, J.L. Luo, Effects of hydrogen and stress on the
634 electrochemical and passivation behaviour of 304 stainless steel in simulated PEMFC
635 environment, Corros. Sci. 145 (2018) 307–319.
636 [22] D. Chastell, P. Doig, P.E.J. Flewitt, K. Ryan, The influence of stress on the pitting
637 susceptibility of a 12%CrMoV martensitic stainless steel, Corros. Sci. 19 (1979)
638 335-341.

639 [23] S.J. Lennon, F.P.A. Robinson, G.G. Garrett, The influence of applied stress and
640 surface finish on the pitting susceptibility of low alloy turbine disk steels in wet steam,
641 Corrosion. 40 (1984) 409-413.
642 [24] G. Vanboven, W. Chen, R Rogge, The role of residual stress in neutral pH stress
643 corrosion cracking of pipeline steels. Part I: Pitting and cracking occurrence, Acta
644 Materialia 55 (2007) 29-42.
645 [25] A. Turnbull, L.N. McCartney, S. Zhou, A model to predict the evolution of pitting
646 corrosion and the pit-to-crack transition incorporating statistically distributed input
647 parameters, Corros. Sci. 48 (2006) 2084–2105.
648 [26] H. Iwanaga, T. Oki, Effect of applied stress on anodic polarization behavior and
649 pitting corrosion of stainless steel, J. Soc. Mater. Sci. Jpn. 30 (1981) 394-400.
650 [27] V. Vignal, N. Mary, R. Oltra, J. Peultier, A mechanical-electrochemical approach
651 for the determination of precursor sites for pitting corrosion at the microscale, J.
652 Electrochem. Soc. 153 (2006) B352-B357.
653 [28] X. Feng, Y. Zuo, Y. Tang, X. Zhao, X. Lu, The degradation of passive film on
654 carbon steel in concrete pore solution under compressive and tensile stresses,
655 Electrochim. Acta. 58 (2011) 258-263.
656 [29] S. Guo, H.T. Wang, E.H. Han, Computational evaluation of the influence of
657 various uniaxial load levels on pit growth of stainless steel under
658 mechanoelectrochemical interactions, J. Electrochem. Soc. 165 (2018) C515-C523.
659 [30] O. O. Fatoba, R. Leiva-Garcia, S.V. Lishchuk, N.O. Larrosa, R. Akid, Simulation
660 of stress-assisted localised corrosion using a cellular automaton finite element

approach, Corros. Sci. 137 (2018) 83-97.

[31] E.M. Gutman, Mechanochemistry of solid surface, World Scientific Publishing Company, Singapore (1994).

[32] R. Elgaddafi, R. Ahmed, S. Shah, Corrosion of carbon steel in CO2 saturated brine at elevated temperatures, J. Petrol. Sci. Eng.196 (2021) 107638.

[33] Y. Hua, S. Xu, Y. Wang, W. Taleb, J. Sun, L. Zhang, R. Barker, A. Nevillea, The formation of $FeCO_3$ and Fe_3O_4 on carbon steel and their protective capabilities against CO_2 corrosion at elevated temperature and pressure, Corros. Sci. 157 (2019) 392-405.

[34] A. Dugstad, L. Lunde, K. Videm, Parametric study of CO2 corrosion of carbon steel, Corrosion/94, paper no. 14 (Houston, TX: NACE International, 1994).

[35] C. de Waard, U. Lotz, A. Dugstad, Influence of liquid flow velocity on CO_2 corrosion a semi-empirical model, Corrosion/95, paper no. 128 (Houston, TX: NACE International, 1995).

[36] C. de Waard, U. Lotz, Prediction of CO_2 corrosion of carbon steel, Corrosion/93, paper no. 69 (Houston, TX: NACE International, 1993).

[37] A. Ikeda, S. Mukai, M. Ueda, Prevention of CO_2 corrosion of line pipe and oil country tubular goods, Corrosion/84, paper no. 289 (Houston, TX: NACE International, 1984).

[38] C. de Waard, L. Smith, B.D. Craig, The influent of crude oil on well tubing corrosion rates, EUROCORR, 2001.

[39] S. Nesic, J. Postlethwaite, S. Olsen, An electrochemical model for prediction of CO_2 Corrosion, Corrosion/ 95, paper no. 131 (Houston, TX: NACE International,

683 1995).

684 [40] S. Nesic, M. Nordsveen, R. Nyborg, A. Stangeland, A mechanistic model for CO_2
685 corrosion of mild steel in the presence of protective iron carbonate scales – Part II: A
686 numerical experiment, Corrosion. 59 (2003) 489.

687 [41] A. Kahyarian, M. Singer, S. Nesic, Modeling of uniform CO_2 corrosion of mild
688 steel in gas transportation systems: A review, J. Nat. Gas. Sci. Eng. 29 (2016)
689 530-549.

690 [42] A. Valor, F. Caleyo, L. Alfonso, D. Rivas, J.M. Hallen, Stochastic modeling of
691 pitting corrosion: a new model for initiation and growth of multiple corrosion pits,
692 Corros. Sci. 49 (2007) 559-579.

693 [43] A. Anderko, N. Sridhar, D. S. Dunn, A general model for the repassivation
694 potential as a function of multiple aqueous solution species, Corros. Sci. 46 (2004)
695 1583-1612.

696 [44] G. Engelhardt, D. D. Macdonald, Unification of the deterministic and statistical
697 approaches for predicting localized corrosion damage. I. Theoretical foundation,
698 Corros. Sci. 46 (2004) 2755-2780.

699 [45] J.C. Velázquez, F. Caleyo, A. Valor, J.M. Hallen, Predictive model for pitting
700 corrosion in buried oil and gas pipelines. Corrosion. 65 (2009) 332-342.

701 [46] H. Qin, W. Zhou, S. Zhang, Bayesian inferences of generation and growth of
702 corrosion defects on energy pipelines based on imperfect inspection data. Reliab. Eng.
703 Syst. Safe. 144 (2015) 334-342.

704 [47] X. Li, Y. Zhao, W. Qi, J. Wang, J. Xie, H. Wang, L. Chang, B. Liu, G. Zeng, Q.

705 Gao, H. Sun, T. Zhang, F.H. Wang, Modeling of pitting corrosion damage based on
706 electrochemical and statistical methods, J. Electrochem. Soc.166 (2019) C539-C549.
707 [48] R. Sánchez-Tovar, M.T. Montañés, J. García-Antón, Contribution of the flowing
708 conditions to the galvanic corrosion of the copper/AISI 316L coupling in highly
709 concentrated LiBr solutions, Corros. Sci. 68 (2013) 91-100.
710 [49] J. Liu, T. Zhang, W. Zhang, Y.G. Yang, Y.W. Shao, G.Z. Meng, F.H. Wang,
711 Quantitative modeling for corrosion behavior in complex coupled environment by
712 response surface methodology, Acta. Metal. Sin-Engl. 28 (2015) 994-1001.
713 [50] Q.F. Hu, Y.C. Liu, T. Zhang, S.J. Geng, F.H. Wang, Modeling the corrosion
714 behavior of Ni-Cr-Mo-V high strength steel in the simulated deep sea environments
715 using design of experiment and artificial neural network, J. Mater. Sci. Technol. 35
716 (2019) 168–175.
717 [51] D. Nakhaie, A. Kosari, J. Mol, E. Asselin, Corrosion resistance of hot-dip
718 galvanized steel in simulated soil solution: A factorial design and pit chemistry study,
719 Corros. Sci. 164 (2020) 108310.
720 [52] W. Li, B.F.M. Pots, X. Zhong, S. Nesic, Inhibition of CO_2 corrosion of mild steel
721 - Study of mechanical effects of highly turbulent disturbed flow, Corros. Sci. 126
722 (2017) 208-226.
723 [53] Y. Zhao, S.Y. Cao, T. Zhang, J.F. Xie, D.K. Xu, F.H. Wang, A new
724 high-efficiency experimental design for optimizing various flow velocities testing in
725 extremely aggressive formation water, Acta. Metall. Sin. Engl. 32 (2019) 944-950.
726 [54] L.Y. Xu, Y.F. Cheng, An experimental investigation of corrosion of X100

727 pipeline steel under uniaxial elastic stress in a near-neutral pH solution, Corros. Sci.
728 59 (2012) 103–109.
729 [55] P.J.W. Mark, J. Anderson, RSM Simplified: Optimizing processes using response
730 surface methods for design of experiments, second edi, CRC Press, [Place of
731 publication not identified], 2017
732 [56] D.D. Macdonald, A.C. Scott, P. Wentrcek, External reference electrodes for use
733 in high-temperature aqueous systems, J. Electrochem. Soc. 126 (1979) 908-911.
734 [57] ASTM G61-86. Standard Test method for conducting cyclic potentiodynamic
735 polarization measurements for localized corrosion susceptibility of iron-, nickel-, or
736 cobalt-based alloys. 2009.
737 [58] Standard ASTM G-48, Pitting and crevice corrosion resistance of stainless steel
738 and related alloys by the use of ferric chloride solution, method A, in Annual Book of
739 ASTM Standards, vol. 03.02 (West Conshohocken, PA: ASTM, 1992).
740 [59] ASTM G46-94 (2013) Standard guide for examination and evaluation of pitting
741 corrosion, in Annual Book of ASTM Standards, vol. 03.02 (West Conshohocken, PA:
742 ASTM, 2013).
743 [60] T. Zhang, X. L. Liu, Y. W. Shao, G. Z. Meng, F. H. Wang, Corrosion of pure
744 magnesium under thin electrolyte layers, Electrochim. Acta. 53 (2008), 7921-7931.
745 [61] D. D. Macdonald, D. F. Heaney, Effect of variable intensity ultraviolet radiation
746 on passivity breakdown of AISI Type 304 stainless steel, Corros. Sci., 42, 1779
747 (2000).
748 [62] A. Anderko, N. Sridhar, M. A. Jakab. A general model for the repassivation

749 potential as a function of multiple aqueous species. 2. Effect of oxyanions on
750 localized corrosion of Fe–Ni–Cr–Mo–W–N alloys [J]. Corros. Sci. 50 (2008)
751 3629-3647.
752 [63] K. J. Evans, N. Sridhar, B. C. Rollins, S. Chawla, J. A. Beavers, J. Page,
753 Long-term evolution of corrosion potential of carbon steel in alkaline radioactive
754 waste environments, Corrosion. 75 (2018) 106-119.
755 [64] G. T. Burstein, R. J. Cinderey, Evolution of the corrosion potential of
756 repassivating aluminium surfaces, Corros. Sci. 33 (1992) 475.
757 [65] R. J. Cinderey, G. T. Burstein, The effects of chromate on the transient
758 repassivation potential of aluminium in chloride solution, Corros. Sci. 33 (1992) 493-
759 498.
760 [66] Y. Zhang, M.U. Macdonald, G.R. Engelhardt. Development of localized
761 corrosion damage on low pressure turbine disks and blades. III: application of damage
762 function analysis to the prediction of damage, Electrochim. Acta. 69 (2012) 19-29.
763 [67] A. Valor, F. Caleyo, D. Rivas, J. M. Hallena, Stochastic approach to
764 pitting-corrosion-extreme modeling in low-carbon steel, Corros. Sci. 52 (2010)
765 910-915.
766 [68] F.A. Almuaili, S.A. McDonald, P.J. Withers, A.B. Cook, D.L. Engelberg,
767 Strain-induced reactivation of corrosion pits in austenitic stainless steel, Corros. Sci.
768 125 (2017) 12-19.
769 [69] J.W. Provan, E.S. Rodriguez III, Part I: Development of a Markov description of
770 pitting corrosion, Corrosion. 45(1989) 178-192.
771 [70] M.K. Cavanaugh, R.G. Buchheit, N. Birbilis. Modeling the environmental

772 dependence of pit growth using neural network approaches, Corros. Sci. 52 (2010)
773 3070-3077.

774

775

776 **List of figures**

794

795 Fig. 7 Cyclic potentiodynamic polarization curves of HP-13Cr SS in simulation
796 formation water at different potential scan rates under various temperatures and CO_2
797 pressures: (a) 95 °C / 2.8 MPa, (b) 120 °C / 3.2 MPa, (c) 150 °C / 3.6 MPa, (d) 180 °C /
798 3.8 MPa

799

800 Fig. 8 E_{pit} (a) and E_{rp} (b) at different potential scan rates (v) for HP-13Cr SS in
801 formation water at different temperatures and CO_2 pressures

802

803 Fig. 9 OCP evolution of HP-13Cr SS in formation water under various temperatures
804 and CO_2 pressures

805

806 Fig.10 Variation of current density (i) with stable pit formation time of HP-13Cr SS in
807 formation water under various temperatures and CO_2 pressures: (a) 95 °C / 2.8 MPa,
808 (b) 120 °C / 3.2 MPa, (c) 150 °C / 3.6 MPa, (d) 180 °C / 3.8 MPa

809

810 Fig. 11 Variation of pit induction time with ΔE (E_{app} - E_{rp}) of HP-13Cr SS under
811 various temperatures and CO_2 pressures: (a) 95 °C / 2.8 MPa, (b) 120 °C / 3.2 MPa, (c)
812 150 °C / 3.6 MPa, (d) 180 °C / 3.8 MPa

813

814 Fig.12 Pit initiation time of HP-13Cr SS in formation water under various
815 temperatures and CO_2 pressures: (a) 95 °C / 2.8 MPa, (b) 120 °C / 3.2 MPa, (c) 150 °C

816 / 3.6 MPa, (d) 180 ºC / 3.8 MPa

817

818 Fig.13 Variety of pit initiation time of HP-13Cr SS in formation water with well depth

819

820 Fig. 14 Cumulative probability and Gumbel plot of maximum pit depth for HP-13Cr
821 SS after pre-initiated pits

822

823 Fig. 15 Typical morphologies of maximum pits for HP-13Cr SS after pre-initiated.

824

825 Fig. 16 Gumbel plots of maximum pit depth for HP-13Cr SS under different
826 immersion time after pre-initiated pits at various temperature and CO_2 pressures: (a)
827 95 ºC / 2.8 MPa, (b) 120 ºC / 3.2 MPa, (c) 150 ºC / 3.6 MPa, (d) 180 ºC / 3.8 MPa

828

829 Fig. 17 Time evolution of the mean maximum pit depth fitted Gumbel distribution at
830 different temperatures and CO_2 pressures

831

832 Fig. 18 The function of pitting growth kinetics parameters K and ω with the well
833 depth

834

835 Fig. 19 Time evolution of the mean maximum pit depth fitted Gumbel distribution at
836 different flow rates

837

838 Fig. 20 Variety of pitting growth kinetics parameters K with flow rate

839

840 Fig. 21 Time evolution of the mean maximum pit depth fitted Gumbel distribution at
841 various (a) tensile stresses, and (b) compressive stresses

842

843 Fig. 22 The function of pitting growth kinetics parameters K (a) and ω (b) with the
844 stress

845

846 Fig. 23 Pareto histogram for weighing the effects of each of the factors on maximum
847 pit depth

848

849 Fig. 24 Six-year-served field data and mechanistic-chemometrics model prediction
850 results for HP-13Cr SS along the well profile

851

852

853

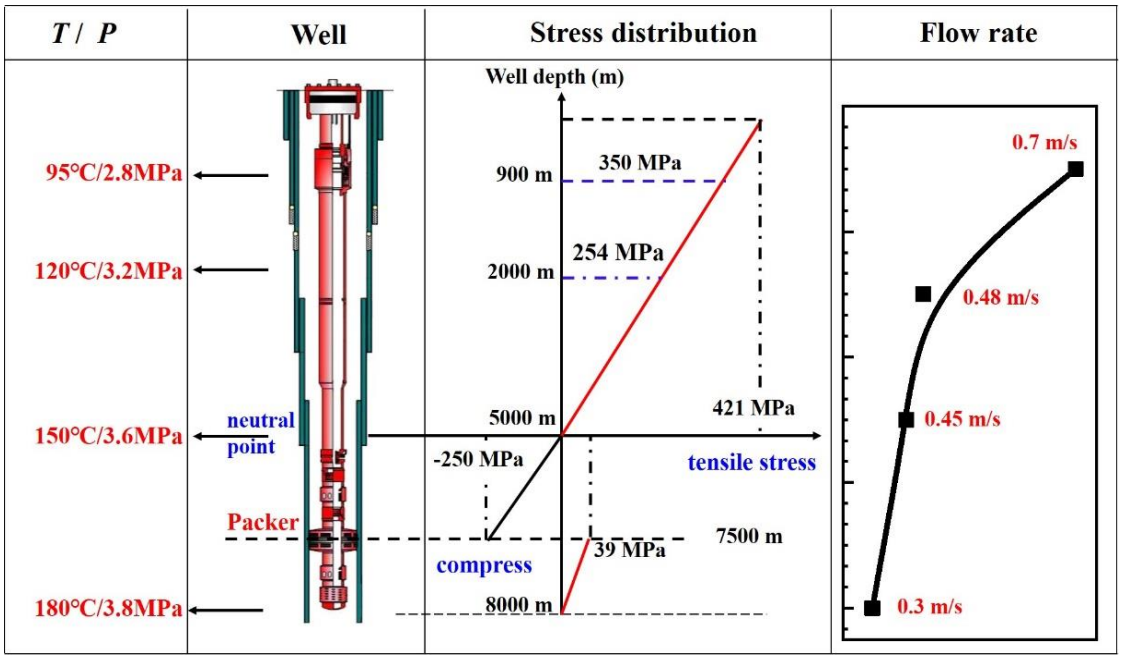

Fig.1 Schematic diagram of complex oilfield environment

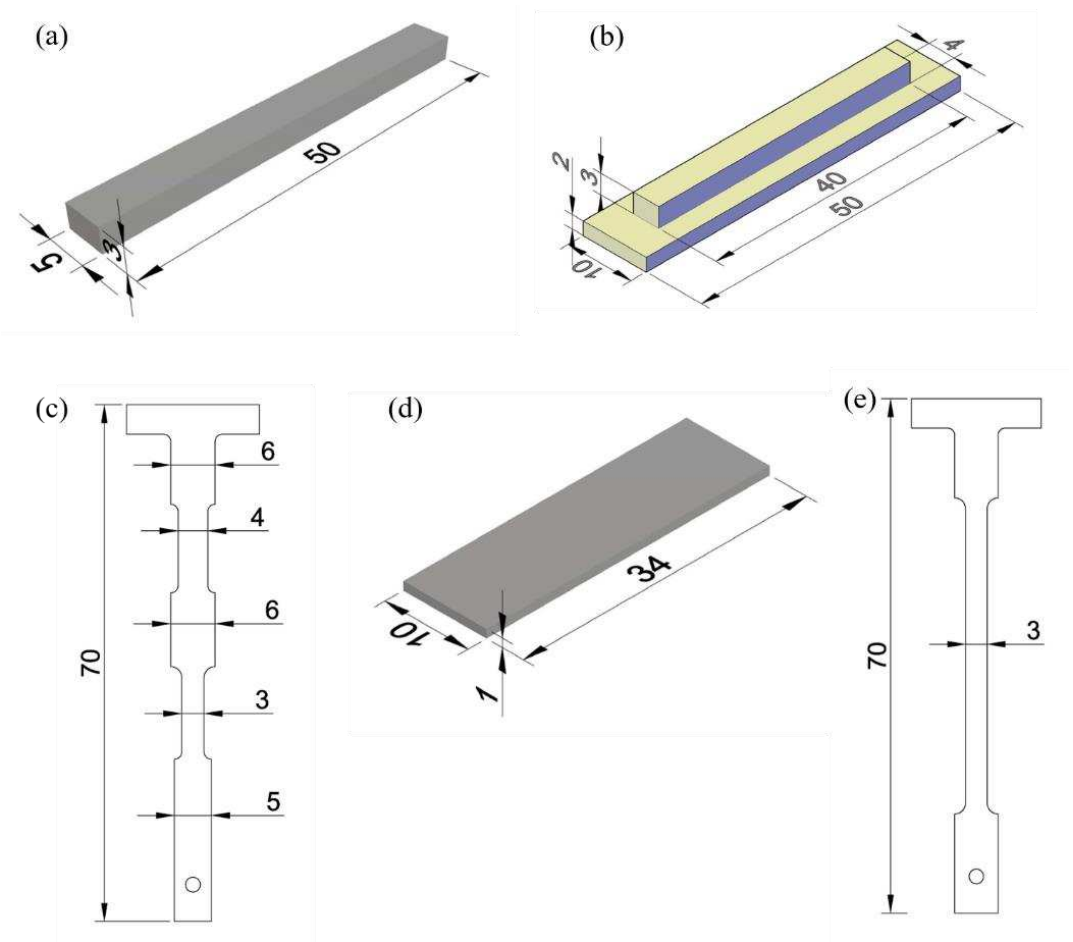

Fig. 2 Dimensions of the testing specimens: (a) Electrochemical and immersion testing specimen, (b) bump-shaped electrode, (c) high throughout tensile stress specimen, (d) compress stress specimen, (e) T-type specimen

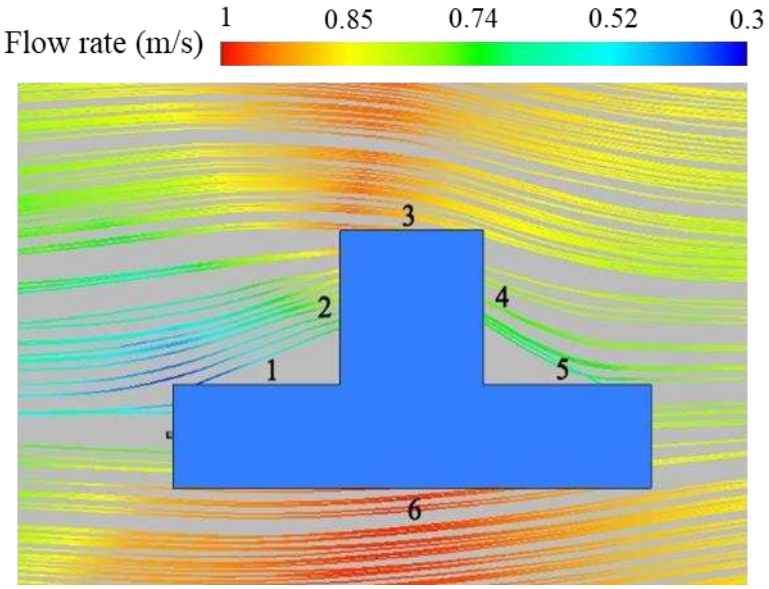

885

886 Fig. 3 Flow rates distribution of the bump-shaped specimen

887
888
889
890
891
892
893
894
895
896
897
898
899
900
901
902
903
904
905
906
907
908
909
910
911
912
913

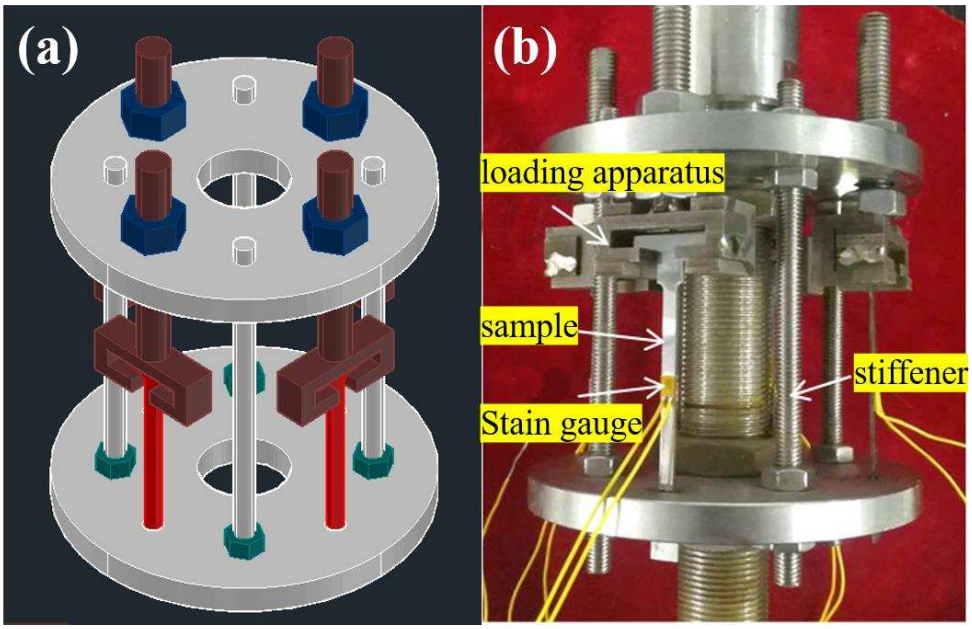

Fig. 4 (a) Schematic diagrams of stress corrosion rotating cage, and (b) specimen assemble

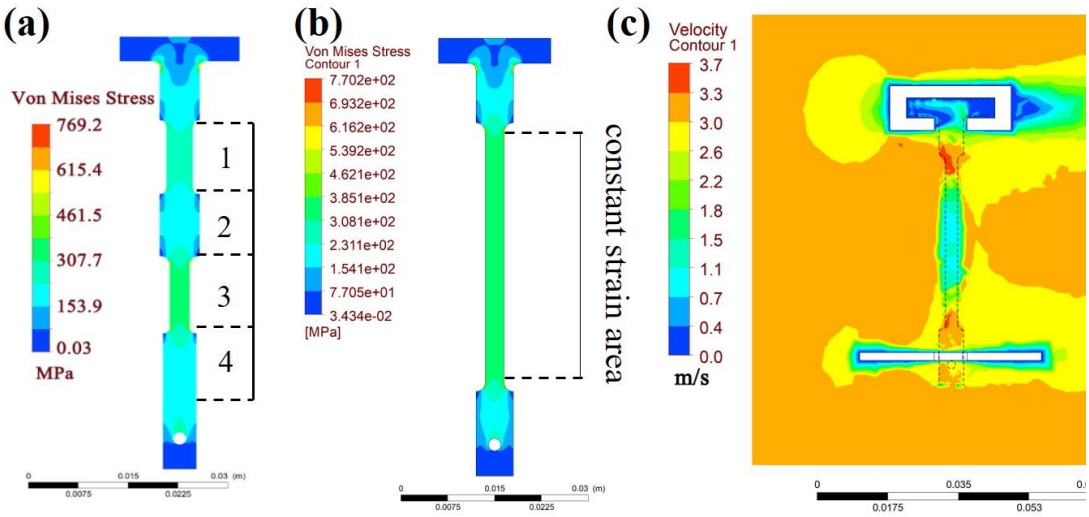

Fig. 5 (a) and (b) von Mises stress distribution of the flat high throughout tensile stress specimen and the T-type specimen, (c) flow distribution around the T-type specimen

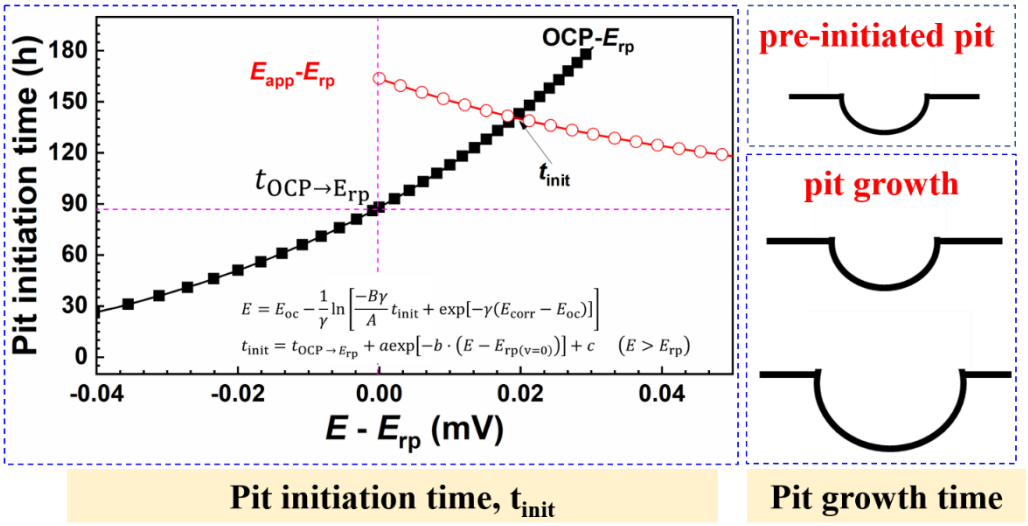

Fig. 6 Schematic of pitting corrosion processes to construct the pitting damage prediction model.

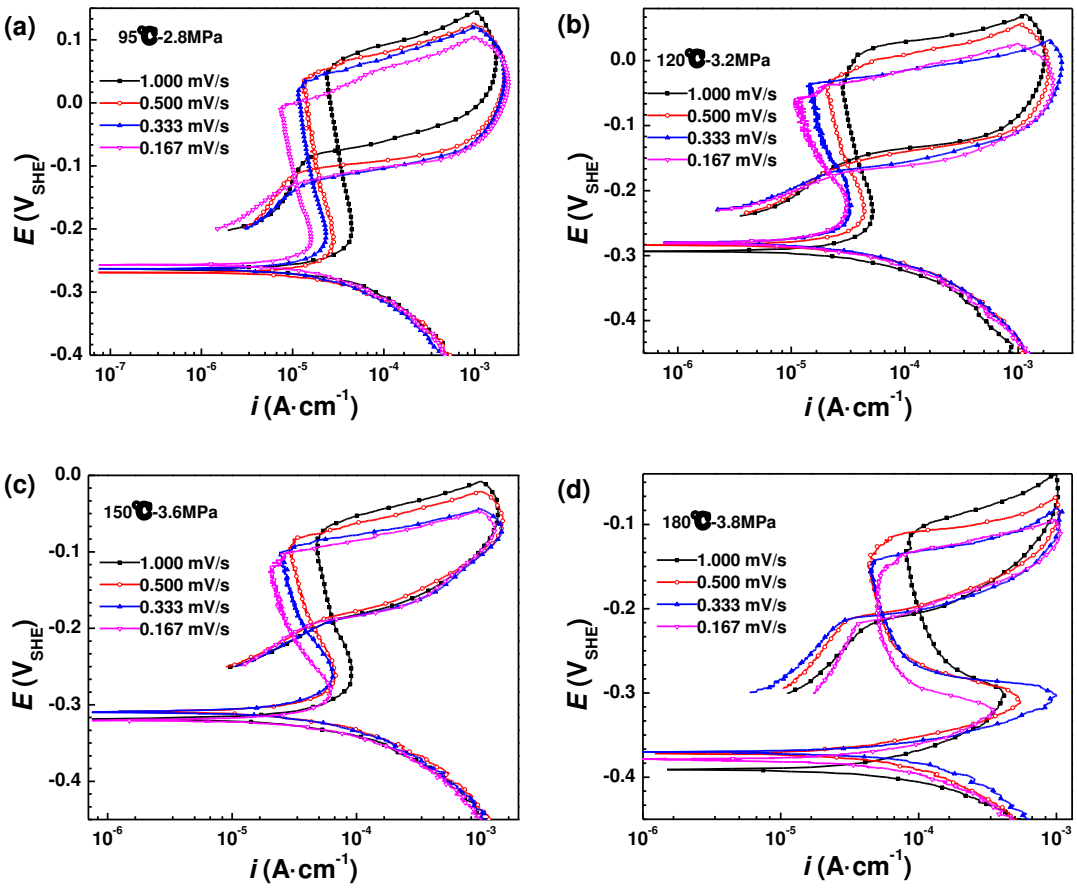

960

961

962 Fig. 7 Cyclic potentiodynamic polarization curves of HP-13Cr SS in simulation

963 formation water at different potential scan rates under various temperatures and CO_2

964 pressures: (a) 95 ºC / 2.8 MPa, (b) 120 ºC / 3.2 MPa, (c) 150 ºC / 3.6 MPa, (d) 180 ºC /

965 3.8 MPa

966

967

968

969

970

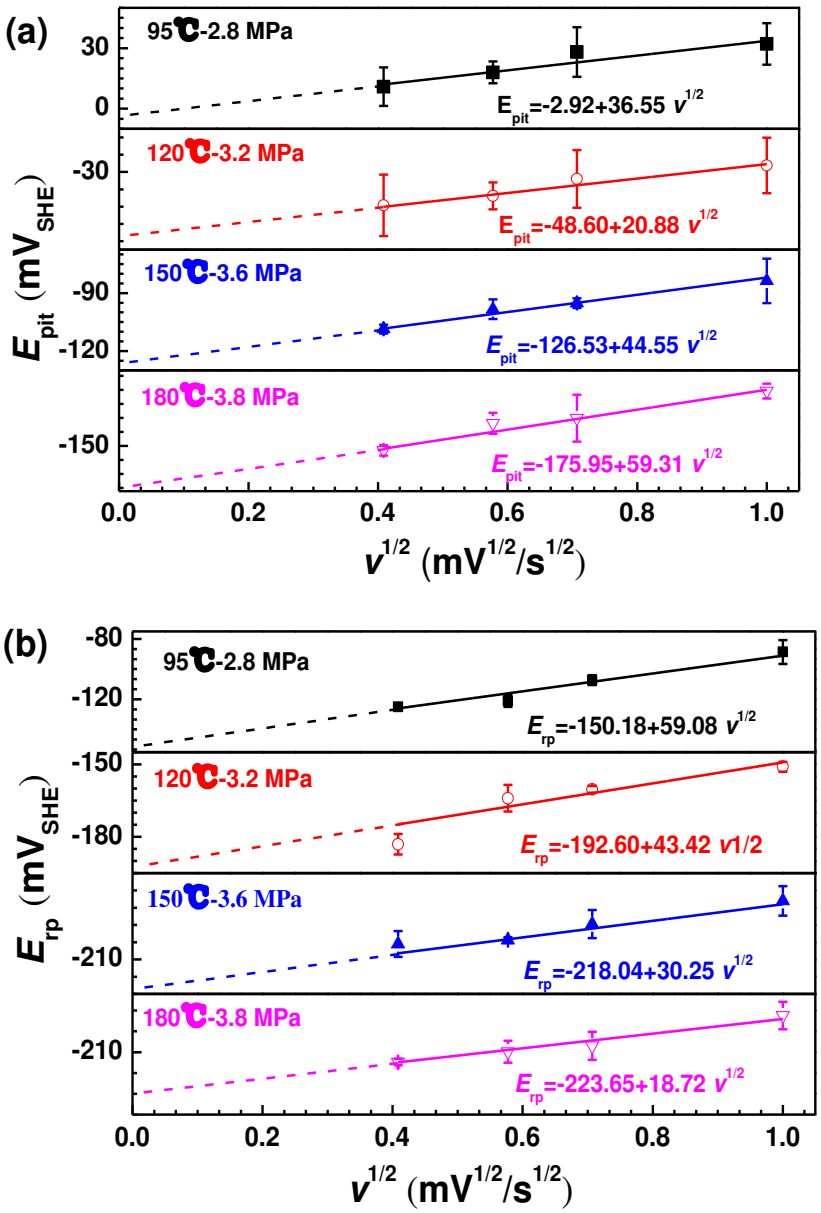

Fig. 8 E_{pit} (a) and E_{rp} (b) at different potential scan rates (v) for HP-13Cr SS in formation water at different temperatures and CO_2 pressures

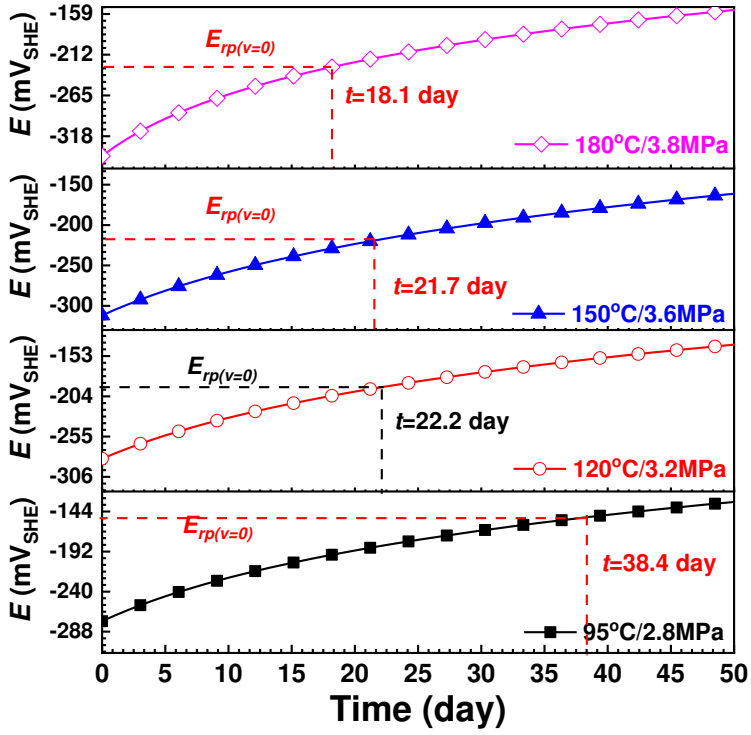

Fig. 9 OCP evolution of HP-13Cr SS in formation water under various temperatures and CO_2 pressures

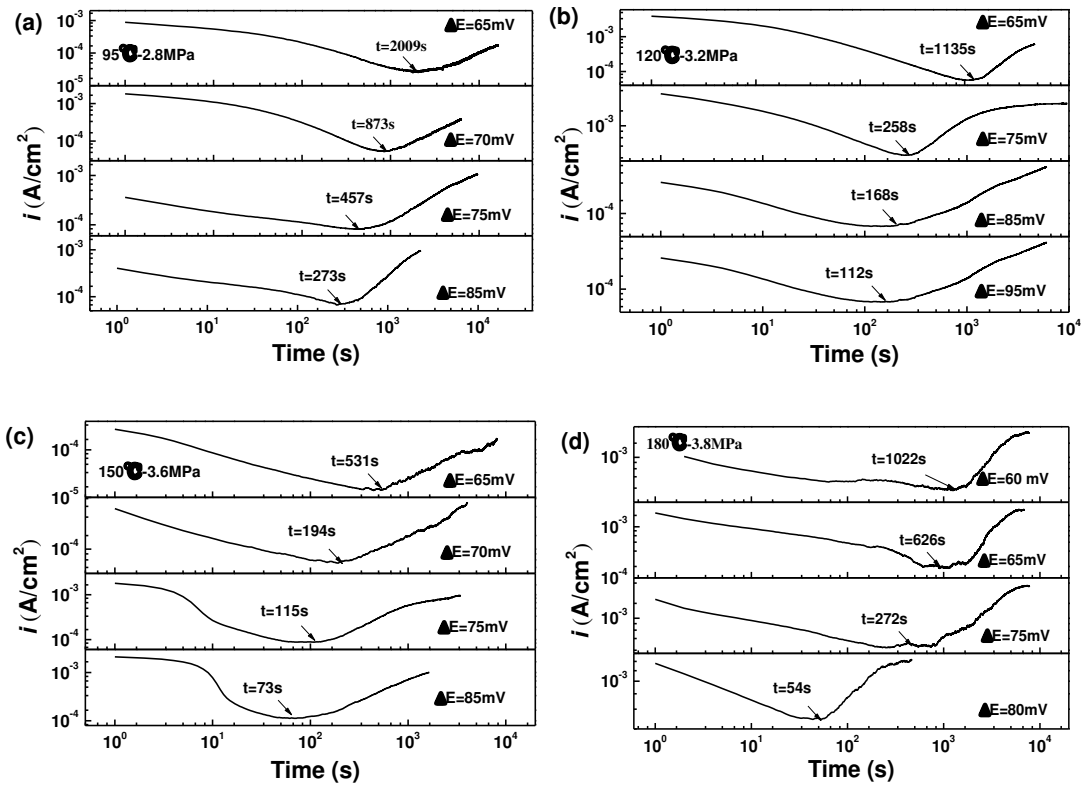

Fig.10 Variation of current density (*i*) with stable pit formation time of HP-13Cr SS in formation water under various temperatures and CO_2 pressures: (a) 95 ºC / 2.8 MPa, (b) 120 ºC / 3.2 MPa, (c) 150 ºC / 3.6 MPa, (d) 180 ºC / 3.8 MPa

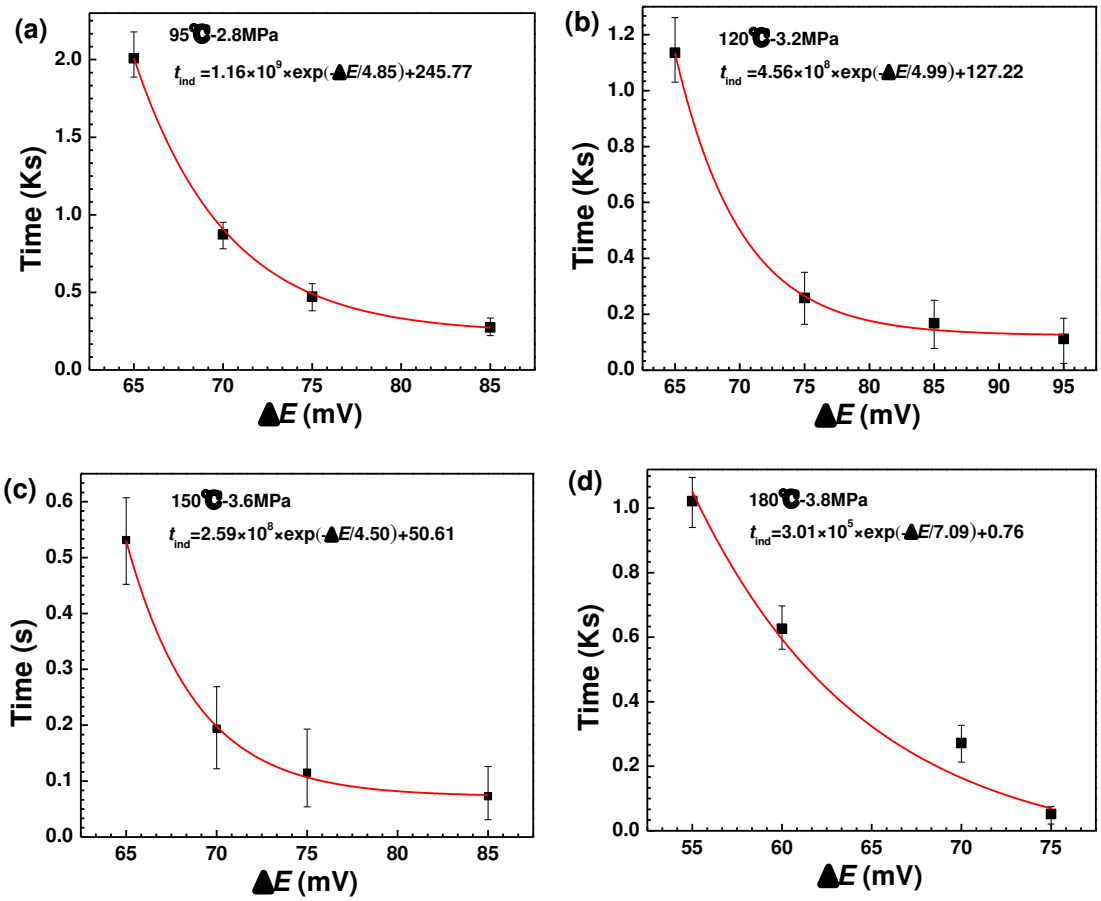

Fig. 11 Variation of pit induction time with ΔE (E_{app} - E_{rp}) of HP-13Cr SS under various temperatures and CO_2 pressures: (a) 95 °C / 2.8 MPa, (b) 120 °C / 3.2 MPa, (c) 150 °C / 3.6 MPa, (d) 180 °C / 3.8 MPa

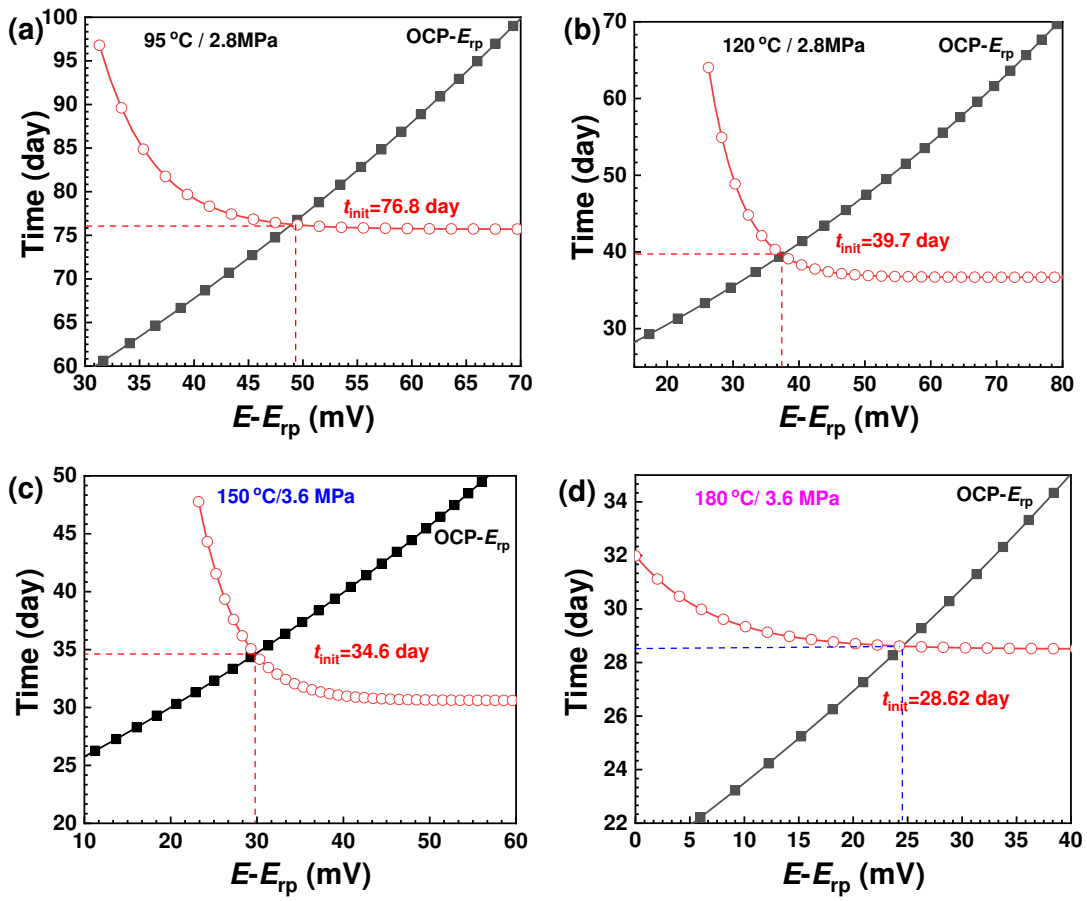

Fig.12 Pit initiation time of HP-13Cr SS in formation water under various temperatures and CO_2 pressures: (a) 95 °C / 2.8 MPa, (b) 120 °C / 3.2 MPa, (c) 150 °C / 3.6 MPa, (d) 180 °C / 3.8 MPa

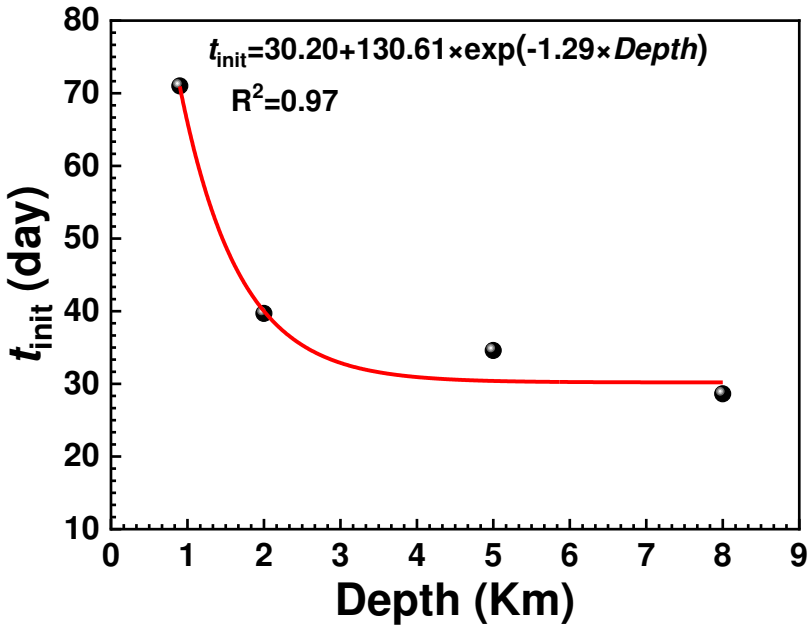

Fig.13 Variety of pit initiation time of HP-13Cr SS in formation water with well depth

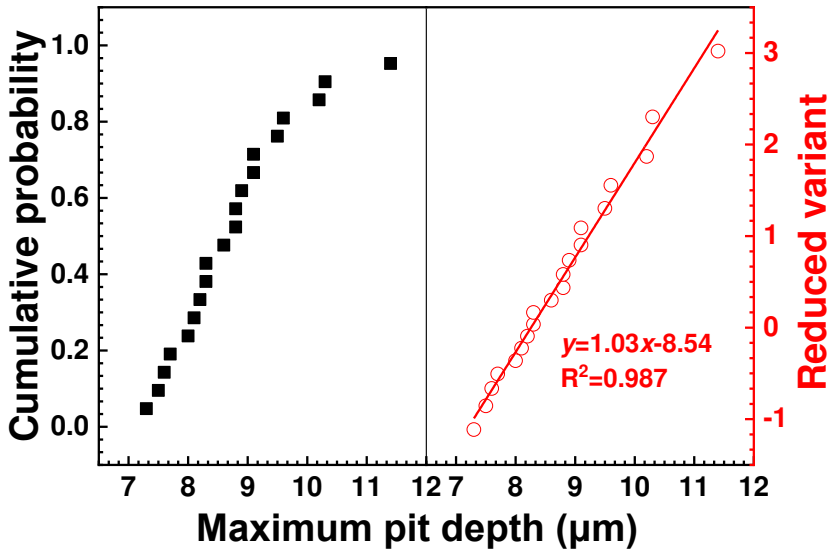

Fig. 14 Cumulative probability and Gumbel plot of maximum pit depth for HP-13Cr SS after pre-initiated pits

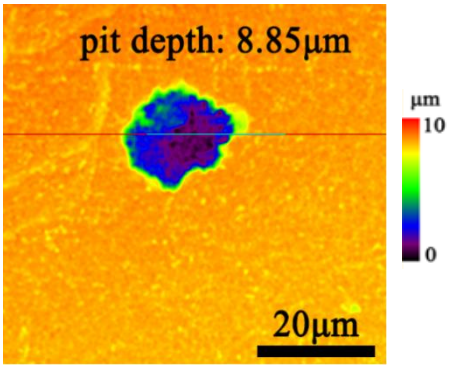

Fig. 15 Typical morphologies of maximum pits for HP-13Cr SS after pre-initiated.

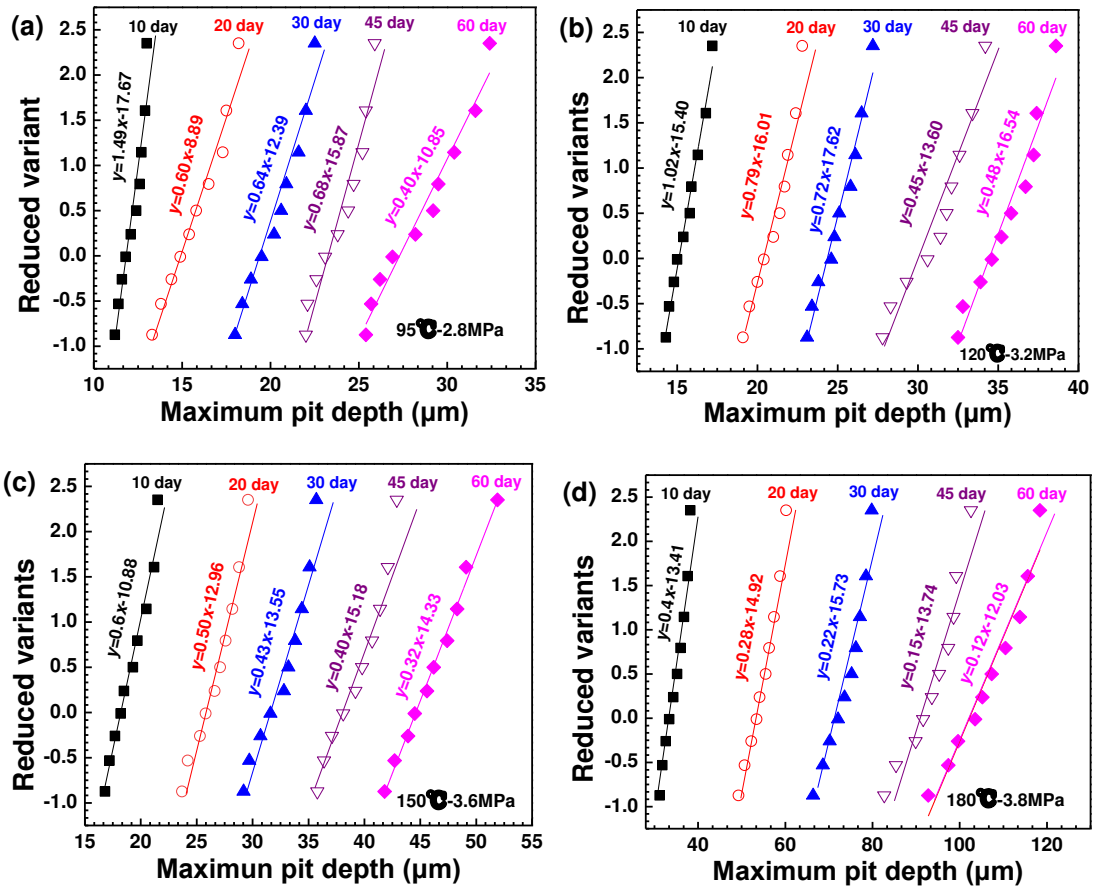

Fig. 16 Gumbel plots of maximum pit depth for HP-13Cr SS under different immersion time after pre-initiated pits at various temperature and CO_2 pressures: (a) 95 ºC / 2.8 MPa, (b) 120 ºC / 3.2 MPa, (c) 150 ºC / 3.6 MPa, (d) 180 ºC / 3.8 MPa

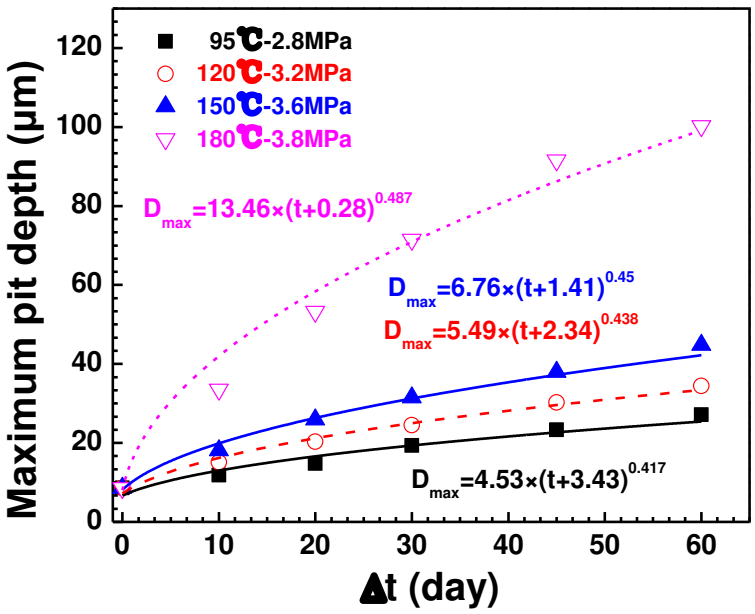

Fig. 17 Time evolution of the mean maximum pit depth fitted Gumbel distribution at different temperatures and CO_2 pressures

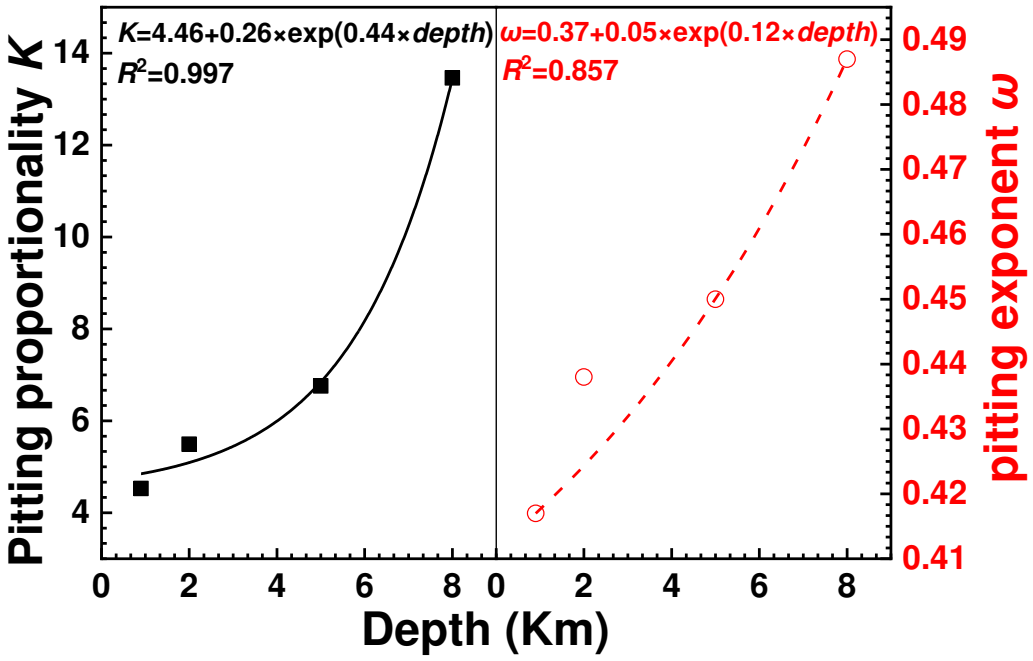

Fig. 18 The function of pitting growth kinetics parameters K and ω with the well depth

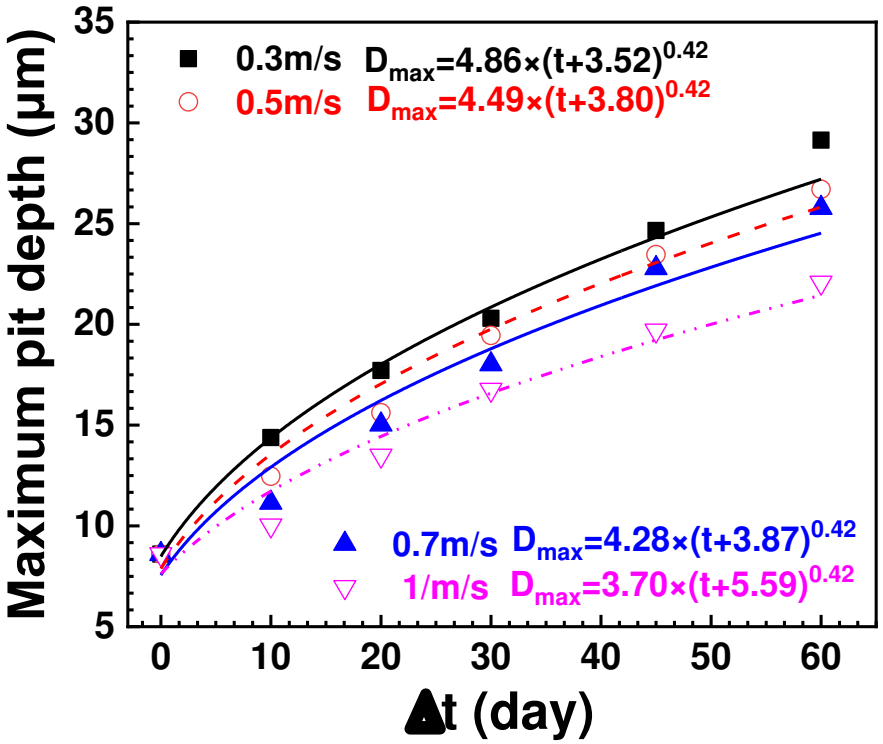

Fig. 19 Time evolution of the mean maximum pit depth fitted Gumbel distribution at different flow rates

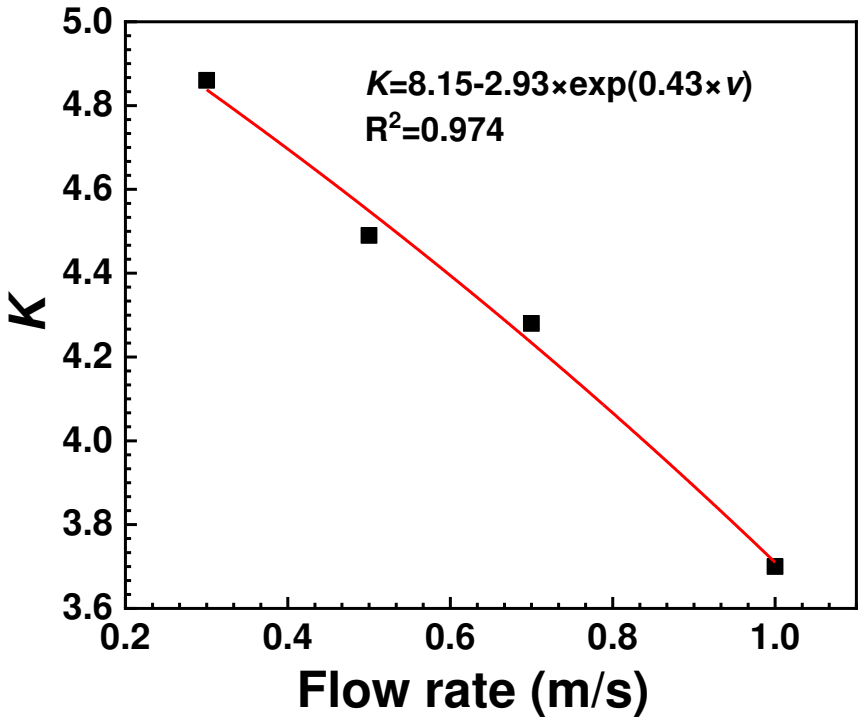

Fig. 20 Variety of pitting growth kinetics parameters *K* with flow rate

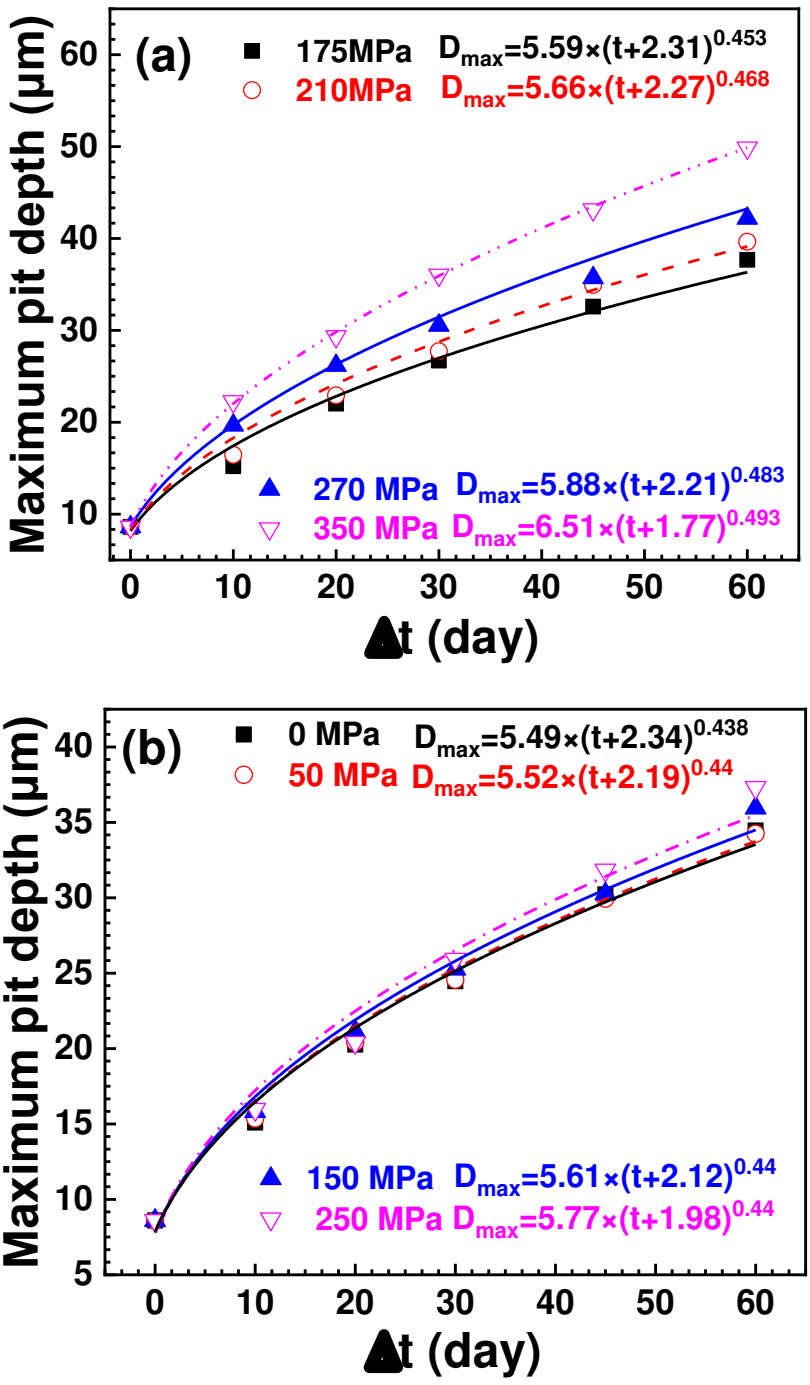

Fig. 21 Time evolution of the mean maximum pit depth fitted Gumbel distribution at various (a) tensile stresses, and (b) compressive stresses

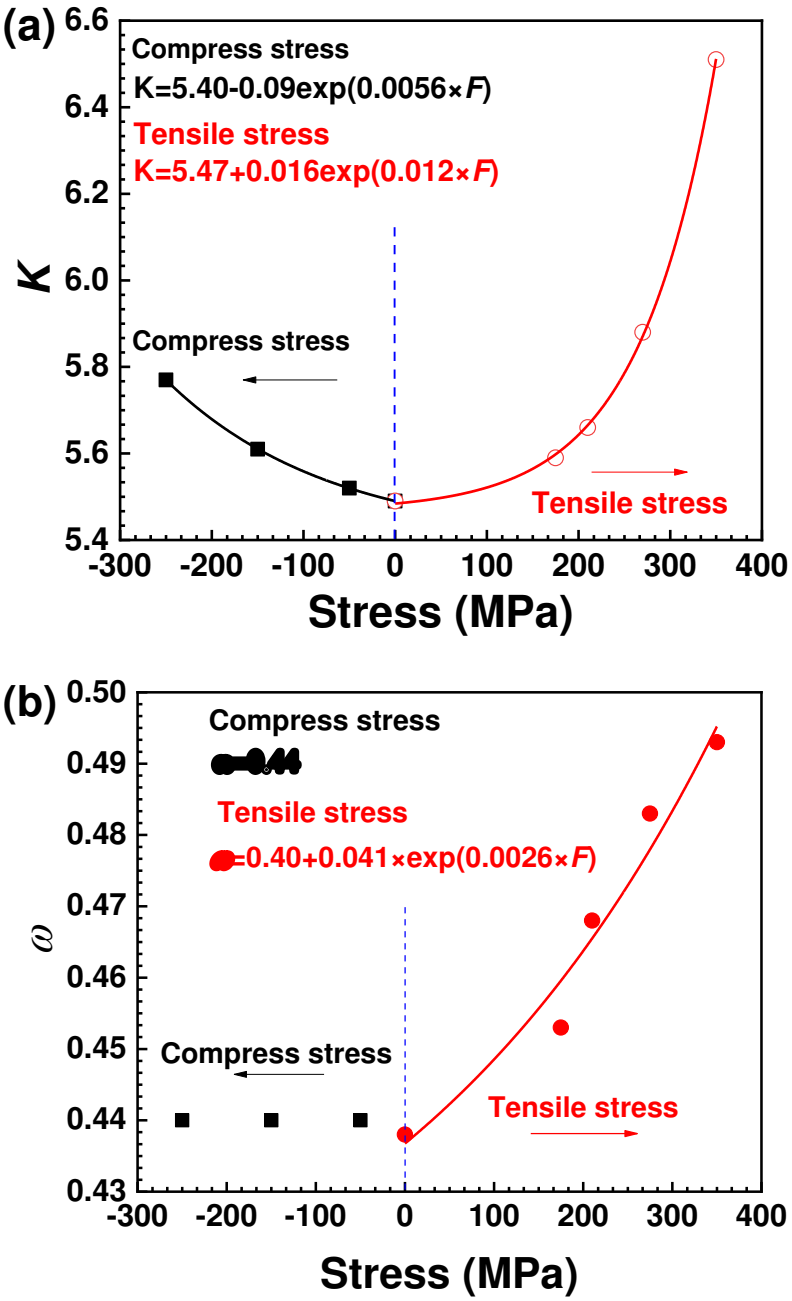

Fig. 22 The function of pitting growth kinetics parameters K (a) and ω (b) with the stress

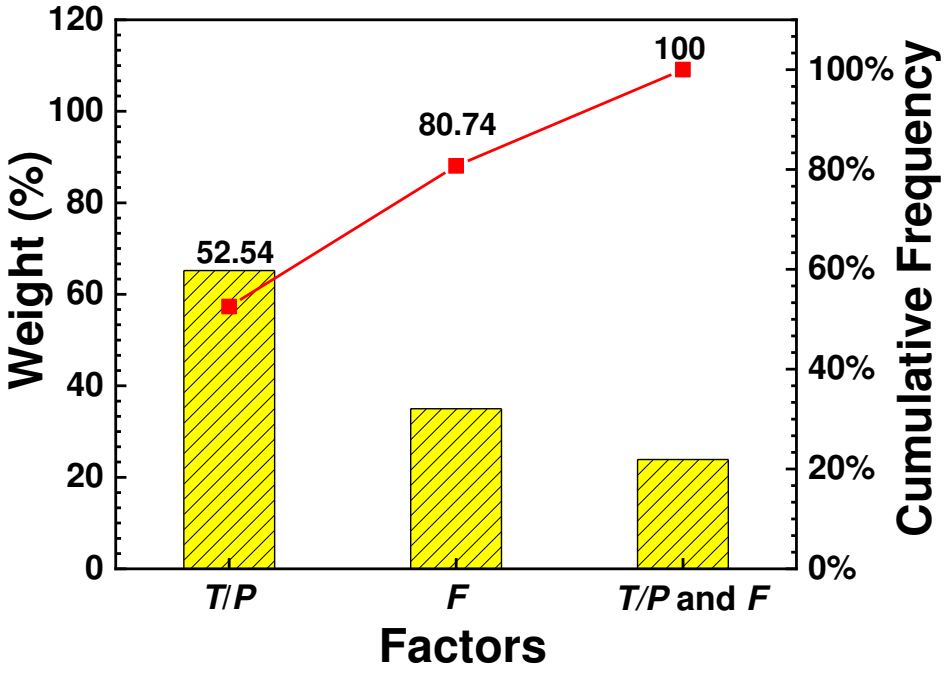

Fig. 23 Pareto histogram for weighing the effects of each of the factors on maximum pit depth

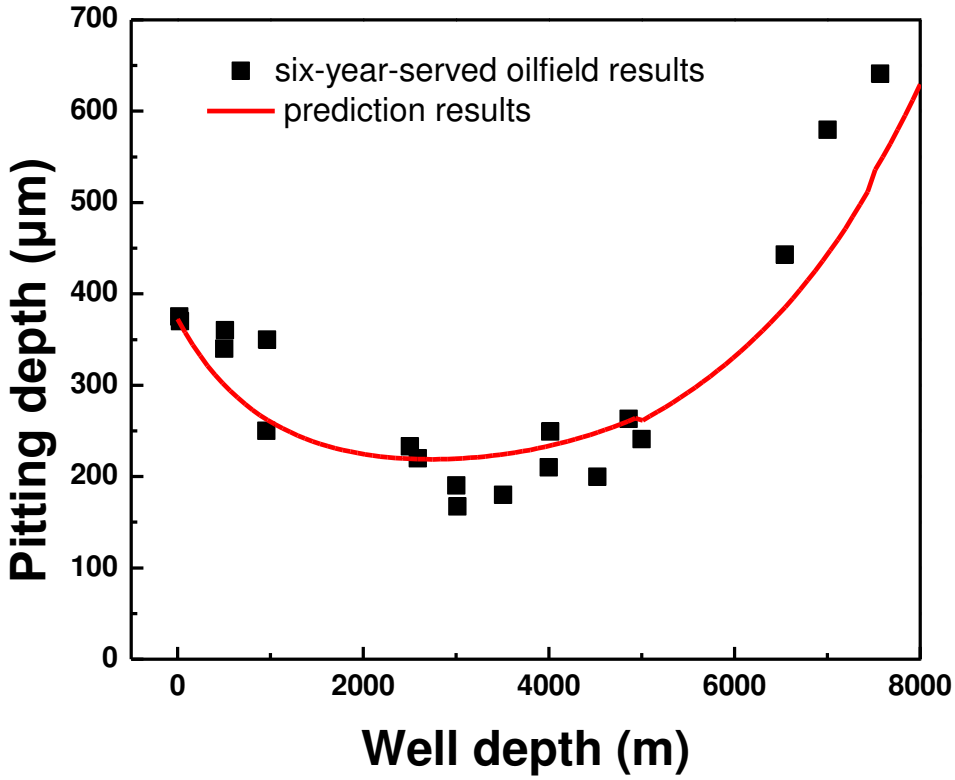

Fig. 24 Six-year-served field data and mechanistic-chemometrics model prediction results for HP-13Cr SS along the well profile.

List of tables

Table 4 The immersion condition of HP-13Cr SS under extremely oilfield environments

Table 5 The value of E_{pit} and E_{rp} at different potential sweep rate (v) under various temperatures and CO_2 pressures

Table 6 Electrochemical parameters to calculate the OCP evolution of HP-13Cr SS under various temperature and CO_2 pressure

Table 7 Gumbel distribution fitting parameters for HP-13Cr SS at different immersion time after pre-initiated pits under various temperature and CO_2 pressure

Table 1 Chemical composition of formation water

Composition	HCO_3^-	Cl^-	SO_4^{2-}	Ca^{2+}	Mg^{2+}	K^+	Na^+
Content (mg L^{-1})	189	60000	430	8310	561	6620	76500

Table 2 Factor values used for factorial design including uncoded and coded form and D_{max} as the response.

Experiment sequence	Factor A (T / P)	Factor B (V)	Factor B (F)	Response (D_{max})			
	°C / MPa	m/s	MPa	μm			
1	95/2.8 (-1)	0.3 (-1)	-250 (-1)	5.59	5.84	5.32	5.74
2	95/2.8 (-1)	0.7 (+1)	-250 (-1)	5.25	5.02	5.65	5.27
3	95/2.8 (-1)	0.3 (-1)	350 (+1)	7.25	7.94	8.94	8.06

4	95/2.8 (-1)	0.7 (+1)	350 (+1)	7.07	7.21	7.66	7.32
5	180/3.8 (+1)	0.3 (-1)	-250 (-1)	13.26	14.82	15.33	15.74
6	180/3.8 (+1)	0.7 (+1)	-250 (-1)	12.28	13.06	12.08	13.28
7	180/3.8 (+1)	0.3 (-1)	350 (+1)	25.03	27.28	28.82	27.22
8	180/3.8 (+1)	0.7 (+1)	350 (+1)	23.37	24.46	25.36	22.44

where temperature / CO_2 pressure represented by T / P, flow rate represented by V, stress represented by F, and the maximum pitting depth represented by D_{max}. Also, -237 MPa in factor represented compress stress, and 350 MPa represent tensile stress.

Table 3 Flow rate for each surface of the bump-shaped specimen

	1	2	3	4	5	6
Flow rate (m/s)	0.31	0.72	0.85	0.66	0.50	1

Table 4 The immersion condition of HP-13Cr SS under extremely oilfield environments

Number	Temperature (℃)/ Pressure (MPa)	Velocity (m/s)	Stress (MPa)
1	95 ºC/2.8 MPa	0	0
2	120 ºC/3.2 MPa	0	0
3	150 ºC/3.6 MPa	0	0
4	180 ºC/3.8 MPa	0	0

5	120 ºC/3.2 MPa	0.31	0
6	120 ºC/3.2 MPa	0.50	0
7	120 ºC/3.2 MPa	0.72	0
8	120 ºC/3.2 MPa	1	0
9	120 ºC/3.2 MPa	0	175
10	120 ºC/3.2 MPa	0	210
11	120 ºC/3.2 MPa	0	270
12	120 ºC/3.2 MPa	0	350

Table 5 The value of E_{pit} and E_{rp} at different potential sweep rate (v) under various temperatures and CO_2 pressures

	v (mV/s)	95 ºC/2.8 MPa	120 ºC/3.2 MPa	150 ºC/3.6 MPa	180 ºC/3.8 MPa
E_{pit}	1.000	32.04 ± 10.29	-28.08 ± 8.03	-83.69 ±11.5	-117.39 ±4.42
(mV_{SHE})	0.500	28.08 ± 12.26	-32.03 ± 8.34	-95.2 ±2.48	-133.53 ±13.99

	0.333	17.98 ± 5.39	-36.94 ± 3.89	-98.37 ±5.06	-136.57 ± 6.27
	0.167	10.89 ± 9.58	-39.61 ± 8.89	-108.63 ±2.32	-152.66 ±3.13
	0	-2.92	-48.60	-126.53	-175.95
E_{rp} (mV_{SHE})	1.000	-88.67 ± 7.83	-150.96 ± 2.05	-193.01 ± 4.29	-201.21 ± 3.31
	0.500	-107.28 ± 3.25	-160.34 ± 1.42	-199.73 ± 4.07	-208.48 ± 3.39
	0.333	-121.07 ± 3.91	-164.05 ± 5.52	-204.37 ± 0.81	-209.89 ± 2.62
	0.167	-125.07 ± 2.34	-183.1 ± 4.21	-205.51 ± 3.74	-212.38 ± 0.78
	0	-150.18	-192.60	-218.04	-223.65

Table 6 Electrochemical parameters to calculate the OCP evolution of HP-13Cr SS under various temperature and CO_2 pressure

	γ ($mV \cdot dec^{-1}$)	i_o ($A \cdot cm^{-2}$)	E_{oc} (mV)	ε_L ($V \cdot cm^{-1}$)	E_{corr} (mV)
95 °C / 2.8 MPa	-89.36	4.93×10^{-5}	-182.7	7.38×10^{3}	-275.6
120 °C / 3.2	-92.67	5.99×10^{-5}	-155.1	6.04×10^{3}	-282.4

MPa									
150	ºC	/	3.6	-97.37	4.11×10^{-5}		4.96×10^{3}		
						-117.0			-312.1
MPa									
180	ºC	/	3.8	-91.07	2.28×10^{-5}		84		
						-72.8			-344.5
MPa									

Table 7 Gumbel distribution fitting parameters for HP-13Cr SS at different immersion time after pre-initiated pits under various temperature and CO_2 pressure

Temperature and CO_2 pressure	Time (day)	Scale parameter (λ)	Local parameter (μ) μm
95 ℃ / 2.8 MPa	10	0.67	11.85
	20	1.66	14.82
	30	1.56	19.36
	45	1.47	23.34
	60	2.50	27.13
120 ℃ / 3.2 MPa	10	0.98	15.10
	20	1.27	20.27
	30	1.39	24.47
	45	2.22	30.22
	60	2.08	34.46
150 ℃ / 3.6 MPa	10	1.67	18.13
	20	2.00	25.92
	30	2.33	31.51
	45	2.50	37.95
	60	3.13	44.78
180 ℃ / 3.8 MPa	10	0.25	33.53
	20	3.57	53.29
	30	4.55	71.50
	45	6.67	91.6
	60	8.33	100.25